ACS NANO
Cite This: ACS Nano 2018, 12, 8145–8159
www.acsnano.org

ARTICLE

Bright Near-Infrared Aggregation-Induced Emission Luminogens with Strong Two-Photon Absorption, Excellent Organelle Specificity, and Efficient Photodynamic Therapy Potential

Zheng Zheng,[†,⊥] Tianfu Zhang,[†,⊥] Haixiang Liu,[†,⊥] Yuncong Chen,[†] Ryan T. K. Kwok,[†] Chao Ma,[‡] Pengfei Zhang,[†] Herman H. Y. Sung,[†] Ian D. Williams,[†] Jacky W. Y. Lam,[†] Kam Sing Wong,[‡] and Ben Zhong Tang*[,†,§,∥]

[†]Department of Chemistry, Hong Kong Branch of Chinese National Engineering Research Center for Tissue Restoration and Reconstruction, Institute for Advanced Study, Department of Chemical and Biological Engineering and Division of Life Science, The Hong Kong University of Science and Technology (HKUST), Clear Water Bay, Kowloon, Hong Kong, China

[‡]Department of Physics, HKUST, Clear Water Bay, Kowloon, Hong Kong, China

[§]HKUST-Shenzhen Research Institute, No. 9 Yuexing First Road, South Area, Hi-Tech Park, Nanshan, Shenzhen 518057, China

[∥]NSFC Center for Luminescence from Molecular Aggregates, SCUT-HKUST Joint Research Institute, State Key Laboratory of Luminescent Materials and Devices, South China University of Technology, Guangzhou 510640, China

Supporting Information

ABSTRACT: Far-red and near-infrared (NIR) fluorescent materials possessing the characteristics of strong two-photon absorption and aggregation-induced emission (AIE) as well as specific targeting capability are much-sought-after for bioimaging and therapeutic applications due to their deep penetration depth and high resolution. Herein, a series of dipolar far-red and NIR AIE luminogens with a strong push−pull effect are designed and synthesized. The obtained fluorophores display bright far-red and NIR solid-state fluorescence with a high quantum yield of up to 30%, large Stokes shifts of up to 244 nm, and large two-photon absorption cross-sections of up to 887 GM. A total of three neutral AIEgens show specific lipid droplet (LD)-targeting capability, while the one with cationic and lipophilic characteristics tends to target the mitochondria specifically. All of the molecules demonstrate good biocompatibility, high brightness, and superior photostability. They also serve as efficient two-photon fluorescence-imaging agents for the clear visualization of LDs or mitochondria in living cells and tissues with deep tissue penetration (up to 150 μm) and high contrast. These AIEgens can efficiently generate singlet oxygen upon light irradiation for the photodynamic ablation of cancer cells. All of these intriguing results prove that these far-red and NIR AIEgens are excellent candidates for the two-photon fluorescence imaging of LDs or mitochondria and organelle-targeting photodynamic cancer therapy.

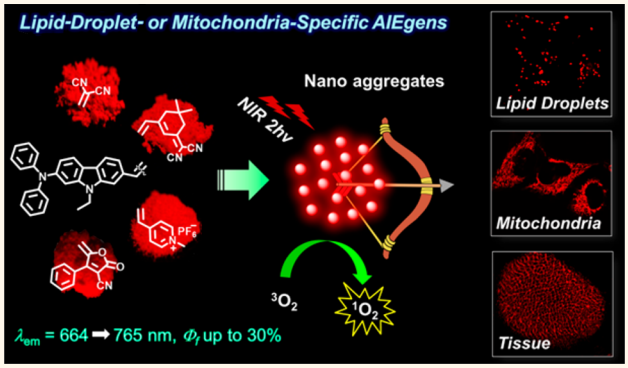

KEYWORDS: *aggregation-induced emission, two-photon absorption, near-infrared emission, organelle-specific imaging, photodynamic therapy*

Bioimaging is related to methods that can non-invasively visualize structural and functional processes in biological systems.[1] In recent decades, the increasing demand for bioimaging tools, particularly for biomedical research and medical applications, has resulted in the development of many advanced techniques, such as magnetic resonance imaging,

Received: April 26, 2018
Accepted: August 3, 2018
Published: August 3, 2018

DOI: 10.1021/acsnano.8b03138
ACS Nano 2018, 12, 8145–8159

computed tomography, positron emission tomography, *etc.*[1−3] However, the high cost of these techniques, unsatisfied spatial resolution, low specificity, poor biocompatibility, and various technological barriers impair their widespread use for routine imaging in medical and specialized research. Fluorescence imaging is a superior alternative to the above imaging techniques and has become a powerful tool for highly sensitive and noninvasive visualization of bioanalytes, biological structures, and processes in real time with high spatial resolution.[4−9] Compared to visible light, far-red and near-infrared (NIR) (650−1000 nm) irradiation is more advantageous for biological imaging for its lesser photodamage to cells, lower scattering, deeper light penetration, and better separation from medium autofluorescence.[10−13] Thus, fluorescent probes with both excitation and emission in the far-red and NIR region are ideal candidates for biological applications.[14−16] Actually, a number of organic fluorophores such as cyanine derivatives, BODIPY derivatives, squaraine derivatives, and phthalocyanines and porphyrin derivatives have been found to possess such optical properties.[17−19] However, these fluorophores often suffer from several intrinsic drawbacks including a small Stocks shift, low solubility and fluorescence quantum yield in aqueous system, nonspecific targeting *in vivo*, and poor photostability and chemical stability.[18] Besides, these conventional far-red and NIR fluorophores are usually planar in structures with extended π conjugation, and such characteristics prone to make them to form aggregates at concentrated solution or in the solid state to result in emission quenching. This effect is known as aggregation-caused quenching (ACQ) and possess another critical obstacle of using conventional far-red and NIR fluorophores as fluorescent probes in bioimaging.[20] Therefore, there is a great demand of far-red and NIR fluorophores that show no these pivotal drawbacks for high-quality bioimaging.

Aggregation-induced emission (AIE) is an opposite phenomenon of ACQ and was originally proposed in 2001.[21] The restriction of intramolecular motion (RIM) was identified as the main reason for this AIE effect.[21−25] Guided by the RIM mechanism, a number of far-red and NIR fluorescent AIE luminogens (AIEgens) with twisted conformation have been developed for various biological applications and have been demonstrated as alternatives to traditional ACQ fluorophores for their higher brightness and increased photostability.[26−32] Generally, for practical use, the majority of far-red and NIR AIEgens was encapsulated into stabilizing matrix such as polyethylene glycol (PEG)-containing amphiphilic polymers because of their inferior water solubility and unsatisfactory cellular uptake.[33,34] In doing so, the constructed nanoparticles exhibit only monotonous functionality. To expand the functionality of nanoparticles, the surface of the fluorescent nanoparticles need to be modified with various functional groups, such as targeting biomolecules, drugs, and genes to make them useful for imaging of complex biological structures and processes and the targeted imaging and treatment of various cancers.[33,35−37] As a promising alternative choice to this complicated nanoparticle engineering, the development of AIEgens, particularly those emitting in the far-red and NIR region, with intrinsic multifunctionality is of great interest but is rarely carried out. It is anticipated that far-red and NIR AIEgens with two-photon excitation show additional advantages in terms of imaging depth and resolution due to the excitation wavelength shift to the biological transparency window (i.e., 700−1000 nm) and the intrinsic confocal nature of the two-photon excitation.[38−40] This ingenious combination of NIR two-photon excitation and NIR emission is especially important for optical *in vivo* deep imaging, such as intravital vasculature and tissue imaging.[40,41]

Lipid droplets (LDs) are intracellular lipid-rich organelles mainly located in adipocytes, hepatocytes, the adrenal cortex, and myocytes and play important roles in regulating the storage and metabolism of neutral lipids, protein degradation, the construction and maintenance of membrane, signal transduction, and so on.[42−47] Although LDs are mainly found in adipose tissue, nearly all cells are capable of storing lipids in these reservoirs because such an ability is crucial for survival.[48,49] Recent studies further reveal that LDs is associated with physiological inflammation and pathologies such as obesity, diabetes, and atherosclerosis as well as viral replication and cancer.[50−55] Mitochondria, however, are another important intracellular organelles responsible for cell respiration and are the primary energy-generating sites in most eukaryotic cells. The mitochondrial dysfunction could induce many types of human diseases such as myopathy, diabetes, and cardiovascular disorders.[56−59] Mitochondria is also emerging as a promising pharmacological target in clinical applications for the detection, inhibition, and treatment of various diseases such as cancer or neurodegenerative diseases, owing to their crucial role in mediating cell apoptosis.[60−62] In particular, mitochondria are regarded as ideal target organelles for therapeutic applications for their biofunctions mentioned above.[63] Therefore, imaging and tracking LDs and mitochondria are important for biological and medical sciences. In recent years, many fluorophores were developed for LD- or mitochondria-specific imaging.[63−68] However, examples of far-red and NIR AIEgens for two-photon excited fluorescence imaging of LDs or mitochondria are still rare.

Structurally, it is well-known that the effective way to red shift the emission of a fluorophore is to increase its push−pull effect and/or effective π conjugation, both of which can also simultaneously improve the two-photon absorption property.[69,70] For the development of far-red and NIR AIEgen, the main challenge is to endow it with a desirable emission wavelength while keeping its AIE feature.[71] The dipolar AIEgens developed previously use phenyl or thiophene rings as the connecting bridge, and most of them exhibit low conjugation and unsatisfactory two-photon absorption.[66,72] Therefore, another challenge is to endow the AIEgen with good two-photon absorption in the biological window through molecular engineering. Thus, it is particularly attractive to develop dipolar AIEgens with a strong push−pull effect and extended conjugation length to simultaneously realize far-red and NIR emission and improved NIR two-photon absorption for various biological applications. Besides, the introduction of various electron-donating groups with different intrinsic nature was also expected to endow the fluorophores with different biological functionalities such as targeting capability.[24] More recently, several studies point out that AIEgens featuring a strong push−pull effect favor the efficient generation of singlet oxygen ($^1O_2$) due to the strong charge transfer, making them serve as photosensitizers (Ps).[37,73] Therefore, designing AIEgens with efficient far-red and NIR emission, strong two-photon absorption, LD- or mitochondria-specific staining capability, and therapeutic effect is of the greatest interest and represents a promising emerging field of research. This will also be the subject of this article.

In this contribution, a series of push−pull AIEgens were designed and synthesized by connecting electron-donating

DOI: 10.1021/acsnano.8b03138
ACS Nano 2018, 12, 8145−8159

Scheme 1. Synthetic Routes to DCMa, DCIs, DCFu, and DCPy[a]

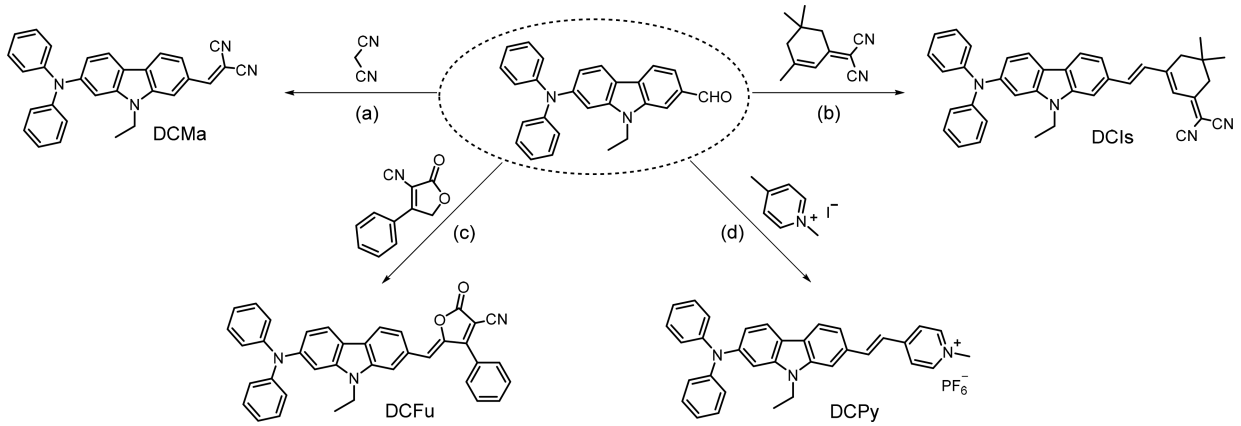

[a]Reagents and conditions: (a) EtOH, reflux, 4 h, 85%; (b) CH_3CN, piperidine, reflux, overnight, 75%; (c) EtOH, reflux, overnight, 85%; (d, i) EtOH, piperidine, reflux, 3 h, 80%; (d, ii) KPF_6, acetone, room temperature, 4 h, 99%.

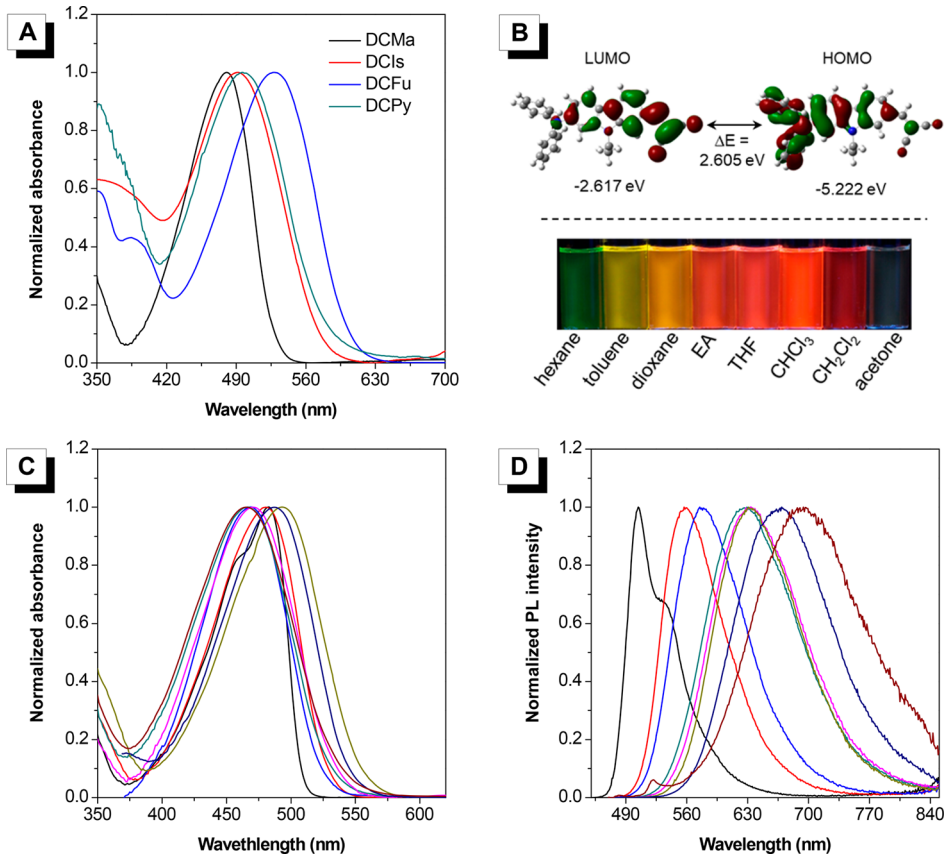

Figure 1. (A) Normalized absorption spectra of DCMa, DCIs, DCFu, and DCPy in toluene solution. (B) Top: molecular orbital amplitude plots of HOMO and LUMO of DCMa calculated at the B3LYP/6-31G (d, p) basis set. Bottom: fluorescent photographs of DCMa in solvents with different polarity taken under 365 nm UV irradiation. (C) Absorption and (D) emission spectra of DCMa in solvents with different polarity: hexane (black line), toluene (red line), dioxane (blue line), ethyl acetate (green line), tetrahydrofuran (magenta line), chloroform (olive line), dichloromethane (navy line), and acetone (brown line).

diphenylamine group to four different electron-withdrawing groups [malononitrile, isophorone, methylpyridinium salt, and 3-cyano-4-phenyl-2(5H)-furanone] through an electron-rich carbazolyl ring (Scheme 1). These AIEgens exhibit bright far-red and NIR emission, robust two-photon absorption, and efficient $^1O_2$ generation. They could specifically stain LDs or mitochondria in living cells and tissues with high brightness and excellent photostability upon one- or two-photon excitation, suggesting their superior performances in two-photon fluorescence imaging of living cells and tissues and organelles-targeted photodynamic ablation of cancer cells.

RESULTS AND DISCUSSION

As depicted in Scheme 1, four carbazole-bridged push−pull AIEgens (namely DCMa, DCIs, DCFu, and DCPy) were originally designed. In the molecules, we perform a molecular

DOI: 10.1021/acsnano.8b03138
ACS Nano 2018, 12, 8145−8159

engineering on the fluorophore structure by employing electron-rich carbazolyl rings to elongate the conjugated system. Further modification on a carbazole core was performed using four different electron-acceptor groups that are end-capped with an electron-donating diphenylamine, which is widely known for enhancing AIE effect.[24] Electron-withdrawing groups include malononitrile, isophorone, methylpyridinium salt, and 3-cyano-4-phenyl-2(5H)-furanone. The various pairs of donors and acceptors were expected to endow the dipolar AIEgens with NIR-active aggregation-induced emission, good two-photon absorption, and impressive therapeutic function.

The key step in the synthesis of compounds DCMa, DCIs, DCFu, and DCPy is the Knoevenagel condensation of 7-(diphenylamino)-9-ethyl-9H-carbazole-2-carbaldehyde with active methylene or methyl acceptors under different conditions. Among them, DCPy further underwent anion exchange to replace iodide with hexafluorophosphate, which avoids the fluorescence quenching effect of iodine atoms. The precursor aldehyde was obtained in two steps starting from ethylation of 2,7-dibromo-9-ethyl-9H-carbazole, followed by formylation reaction under acidic condition (Scheme S1 in the Supporting Information). Four final products were purified by either recrystallization or flash column chromatography in excellent yields of 75−85%. All intermediates and products were fully characterized by NMR and high resolution mass spectrometry (see Figure S1−S18 in the Supporting Information for the details).

After confirmation of the molecular structures of DCMa, DCIs, DCFu, and DCPy, their optical properties were subsequently investigated. As presented in the absorption spectra of the four fluorophores in toluene (Figure 1A), DCMa, DCIs, DCFu, and DCPy show their absorption maximum at 480, 491, 528, and 496 nm, respectively, which are attributed to intramolecular charge transfer (ICT) transition from the electron-donating diphenylamino group to the different type of electron-accepting group. In comparing the absorption spectra of this series of compounds, the gradual bathochromic shift in the order of DCMa < DCIs < DCPy < DCFu should be ascribed to the increasing electron affinity of the acceptor [malononitrile < isophorone < pyridium < 3-cyano-4-phenyl-2(5H)-furanone], which will strengthen the push−pull effect and thereby reduce the energy gaps between excited states and ground states. To better understand the ICT transitions within these fluorophores, we performed density functional theory (DFT) calculations for four fluorophores by using the single-crystal structure determined by X−ray analysis (Figures 1B and S19). The molecular orbital density in the HOMO is mainly located on the diphenylamino moiety and the central carbazole ring, whereas the LUMO level is primarily localized on the acceptor framework, suggesting strong charge-transfer characteristics of fluorophores.

Interestingly, as shown in Figures 1B−D and S20−S23, all of the fluorophores show significant solvent effects. For four fluorophores, their absorption spectra are slightly affected by the polarity of solvents, whereas a remarkable positive solvatochromism on their emission is observed. As shown in Figure 1D, the emission maximum of the representative DCMa has a bathochromic shift from λ_{em} = 504 to 694 nm with increasing solvent polarity from hexane to acetone. In addition, the emission intensity of four fluorophores is greatly reduced or even quenched in polar solvent such as DMSO, suggesting a strong twisted intramolecular charge-transfer (TICT) effect in polar media.

Owing to the strong push−pull dipolar character of compounds DCMa, DCIs, DCFu, and DCPy, interesting nonlinear optical properties and, in particular, two-photon absorption properties can be expected. Thus, the two-photon excitation spectra of four fluorophores were recorded in dioxane (for DCMa, DCIs, and DCFu) and THF (for DCPy) using the two-photon-excited fluorescence (TPEF) method. The emission signals were collected upon excitation from 800 to 1040 nm (at 20 nm intervals), in which compounds have no linear absorption. As shown in Figure 2, this series of compounds

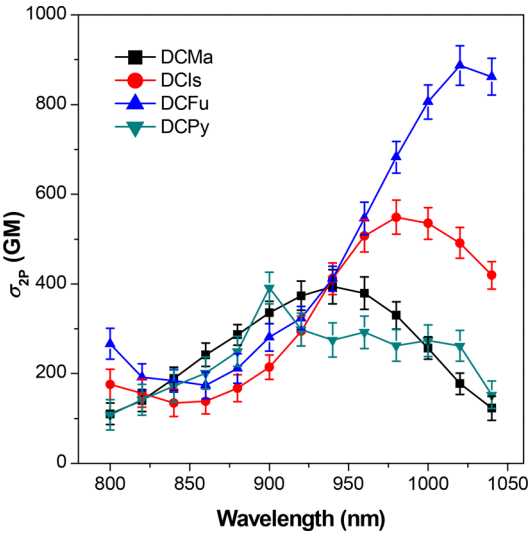

Figure 2. Two-photon absorption cross-section of DCMa, DCIs, DCFu, and DCPy. Solvents: dioxane (DCMa, DCIs, and DCFu) and THF (DCPy). Concentration: 1 × 10^{-4} M.

display excellent two-photon absorption activity in the range of 800−1040 nm. Impressively, DCMa, DCIs, DCFu, and DCPy exhibit a maximum two-photon absorption cross-section (σ_{2P}) of 394, 548, 887, and 390 GM at 940, 980, 1020, and 900 nm, respectively. These results indicate that, for these compounds with the same donor moiety, increasing the strength of electron-withdrawing end-groups results in a pronounced enhancement of the two-photon absorption cross-sections. Compound DCFu, containing the strongest electron-withdrawing group in the series, exhibits a more than 2-fold enhancement of σ_{2P} relative to DCMa and DCPy. Moreover, the σ_{2P} values of the synthesized carbazole-bridged push−pull fluorophores are greatly improved compared with the previously reported values for phenyl-bridged AIEgens and other fluorophores.[66,70,72,74,75] These results strongly demonstrate the design of the conjugated dipolar chromophores for achieving good two-photon absorption activity located at biological transparency window in the range of 700−1000 nm.

The AIE property of DCMa, DCIs, DCFu, and DCPy was studied in acetone−water or DMSO−water mixtures with different water fractions (f_w) (Figures 3 and S24−S27). In pure acetone or DMSO solutions, all of the compounds display weak emission. Upon gradually increasing the water fraction from f_w = 0 to 50 (for DCMa, DCIs, and DCFu) or 80 vol % (for DCPy) (Figure 3B), the fluorescence intensities of the compounds in the mixture solvent are significantly decreased, which are attributed to the inherent TICT effect of push−pull compounds resulting from the increase in solvent polarity by gradually adding water. This result is also in agreement with the

DOI: 10.1021/acsnano.8b03138
ACS Nano 2018, 12, 8145−8159

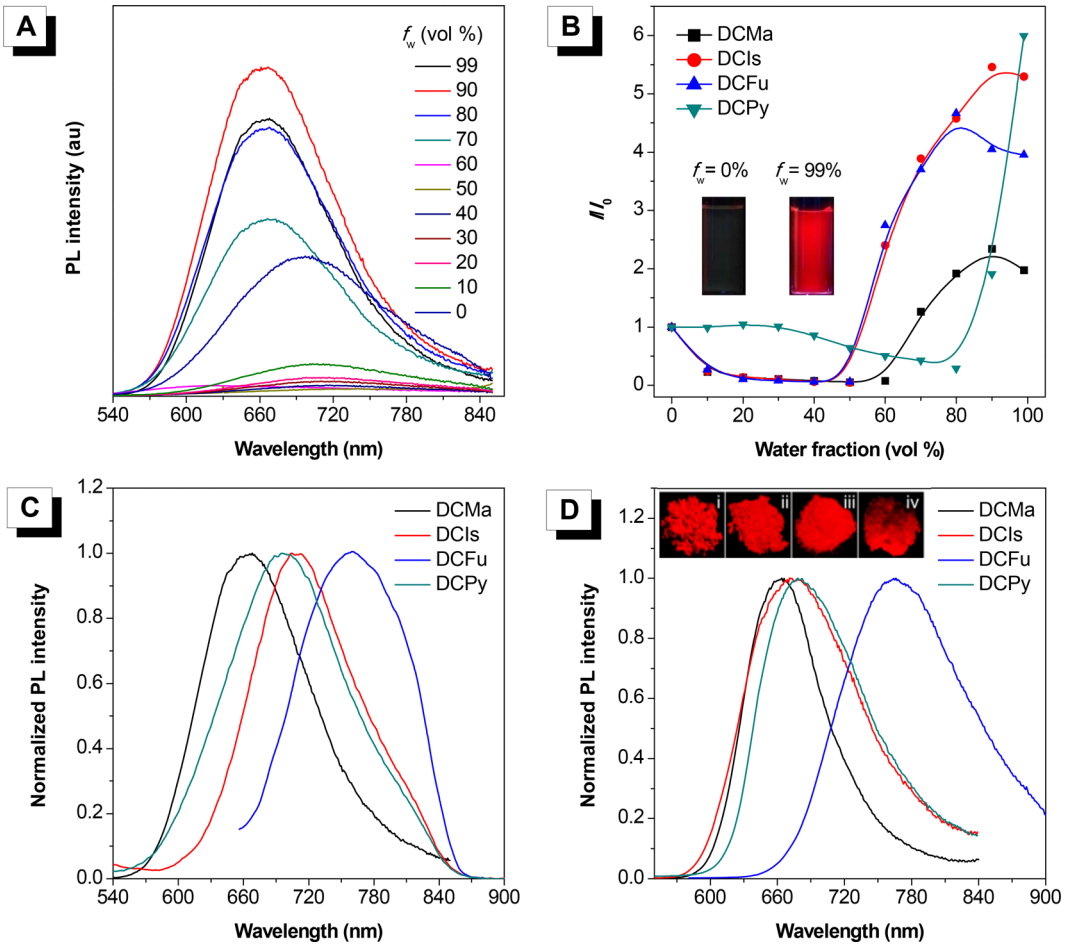

Figure 3. (A) PL spectra of DCMa (10 μM) in acetone−water mixtures with different water fractions (f_w). (B) Plot of relative PL intensity (I/I_0) vs the composition of the acetone−water (DCMa, DCIs, and DCFu) or DMSO−water (DCPy) mixtures. Inset: fluorescent images of DCIs (10 μM) in acetone solution and in acetone−water mixtures with 99% water fraction taken under 365 nm UV irradiation. (C) Normalized PL spectra of DCMa, DCIs, DCFu, and DCPy in the aggregate suspension with 99% water fraction. (D) Normalized PL spectra of DCMa, DCIs, DCFu, and DCPy in the solid state. Inset: fluorescent photographs of (i) DCMa, (ii) DCIs, and (iii) DCPy taken under 365 nm UV irradiation and (iv) DCFu taken using CRI *in vivo* imaging system.

solvatochromic effect of compounds discussed above. Moreover, further increase the f_w results in a remarkable fluorescence enhancement, revealing the AIE feature of DCMa, DCIs, DCFu, and DCPy. In this process, the enhanced emission could be attributed to the formation of the nanoaggregates, which will not suffer from TICT effect in the polar solvent. Simultaneously, rotations in the molecules are greatly restricted in the aggregate state, and thus, the aggregation-induced emission occurs. For compounds DCMa, DCIs, and DCFu, after reaching a maximum intensity at f_w = 80 or 90 vol %, the fluorescence intensity slightly decreases upon further increasing the water fraction f_w. Meanwhile, the decreased and broadened absorption spectra of DCMa, DCIs, DCFu, and DCPy at high f_w also indicative of the formation of nanoscopic aggregates (Figures S24−S27), which is consistent with their emission spectra and AIE behavior. These results indicate that the four designed compounds are AIE active in the far-red and NIR region with the maximum emissions in aggregation state (f_w = 99 vol %) located at 665, 709, 755, and 698 nm for DCMa, DCIs, DCFu ,and DCPy, respectively (Figure 3C and Table 1). Owing to the AIE characteristics, DCMa, DCIs, DCFu, and DCPy show the bright far-red and NIR solid-state fluorescence peaked at 664, 673, 765, and 678 nm, respectively (Figure 3D). The fluorescence quantum yields (Φ_f) of DCMa, DCIs, DCFu, and DCPy in the solid state were measured by integrating sphere to be 29.6%, 13.5%, 1.7%, and 6.9%, respectively. Moreover, time-resolved fluorescence measurements for DCMa, DCIs, DCFu, and DCPy in the solid state reveal that their lifetimes range from 2.62 to 10.05 ns (Table 1 and Figure S28). The above results also demonstrate that the resulting emission color of nanoaggregates and solid can be facilely turned to far-red and NIR region by molecular engineering employing carbazole bridge and different strong acceptors. Moreover, it is interesting to find that all the

Table 1. Optical Properties of DCMa, DCIs, DCFu, and DCPy[a]

	solid state			aggregate		
AIEgen	λ_{em} (nm)	Φ_F (%)	τ_F (ns)	λ_{abs} (nm)	λ_{em} (nm)	$\Delta\nu$ (nm)
DCMa	664	29.6	10.05	478	665	187
DCIs	673	13.5	3.19	510	709	199
DCFu	765	1.7	2.62	538	755	217
DCPy	678	6.9	7.68	454	698	244

[a]Abbreviation: λ_{abs}, absorption maximum and λ_{em}, emission maximum measured in solid-state, acetone−water mixture (1:99, v/v) (DCMa, DCIs, and DCFu), and DMSO−water mixture (1:99, v/v) (DCPy); Φ_F, fluorescence quantum yield determined using an integrating sphere; τ_F, fluorescence lifetime; $\Delta\nu$, Stokes shift, $\lambda_{em} - \lambda_{abs}$.

DOI: 10.1021/acsnano.8b03138
ACS Nano 2018, 12, 8145−8159

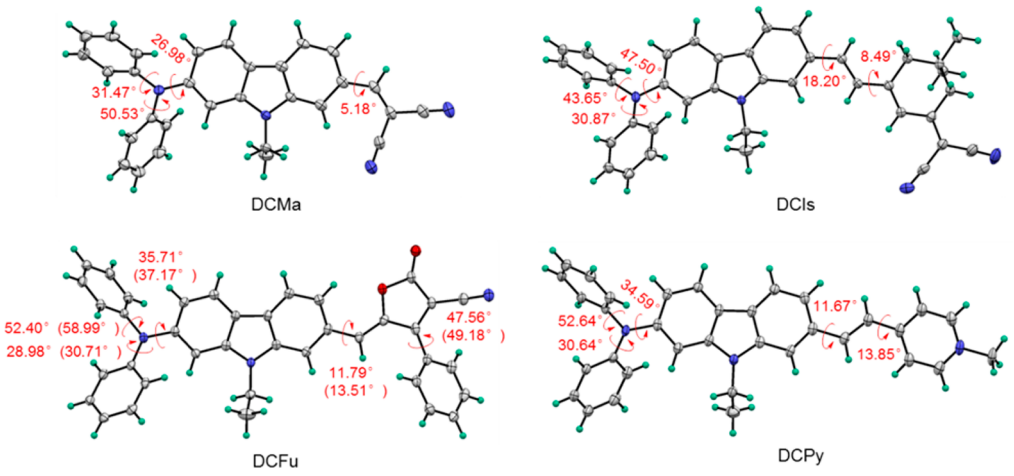

Figure 4. Crystal structures of DCMa (CCDC: 1814852), DCIs (CCDC: 1814845), DCFu (CCDC: 1814843), and DCPy (CCDC: 1814846). The solvent molecules and hexafluorophosphate in DCPy are omitted for clarity.

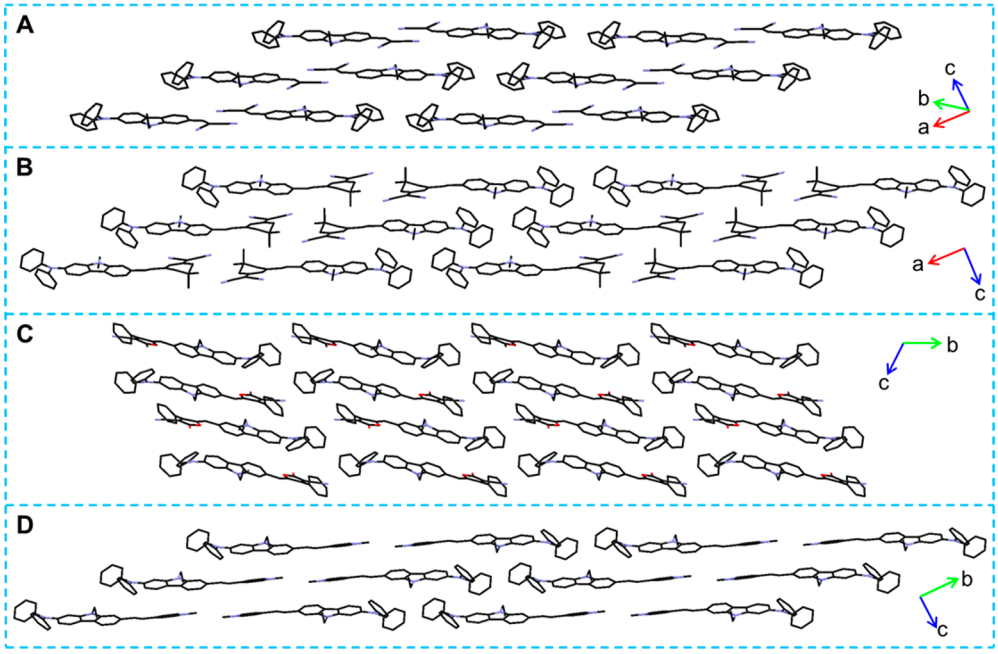

Figure 5. Illustration of crystal packing of (A) DCMa, (B) DCIs, (C) DCFu, and (D) DCPy. The solvent molecules, hexafluorophosphate, and hydrogen atoms are omitted for clarity.

compounds show very large Stokes shifts ($\Delta\nu$ = 187−244 nm), which are favorable for bioimaging due to the minimized interference between excitation and emission.

Besides, it is noteworthy that all of the fluorescent aggregate suspensions at f_w = 99 vol % are transparent and macroscopically homogeneous with no precipitation within at least 1 month, suggesting an excellent colloidal stability of the formed aggregates. The average diameters (D) of nanoaggregates (f_w = 99 vol %) were determined by dynamic light scattering (DLS) measurements to be 65, 87, 81, and 64 nm for DCMa, DCIs, DCFu, and DCPy, respectively (Figure S29). The scanning electron microscopy (SEM) images of representative compounds DCMa and DCFu show that the spherical nanoaggregates were formed in the suspension with the sizes similar to DLS results (Figure S30).

The observations of the AIE effect and bright solid-state fluorescence of compounds triggered us to elucidate their molecular conformation and molecular arrangement in their crystals. Crystals suitable for single crystal X−ray analysis were obtained for compounds DCMa, DCIs, DCFu, and DCPy by slow evaporation from acetonitrile or the ethanol−CH_2Cl_2 mixture solution. Their crystal data and collection parameters are summarized in Tables S1−S4. DCMa, DCIs, and DCFu crystallized in the triclinic $P-1$ space group with an elemental cell containing two (for DCMa and DCIs) or four (for DCFu) molecules, whereas DCPy belongs to the monoclinic $I2/a$ space group with an elemental cell containing eight molecules. Single crystal X−ray diffraction analyses provide direct evidence for the absolute structure of the compounds DCMa, DCIs, DCFu and DCPy. As shown in Figure 4, all compounds exhibit the trans conformation except DCMa, which does not have a conformation isomer. The crystal structures reveal that the carbazole substructure is essentially planar for all four compounds. To further evaluate the planarity of the whole molecule, the various dihedral angles within the molecular backbones were presented for the four compounds. It should be

DOI: 10.1021/acsnano.8b03138
ACS Nano 2018, 12, 8145−8159

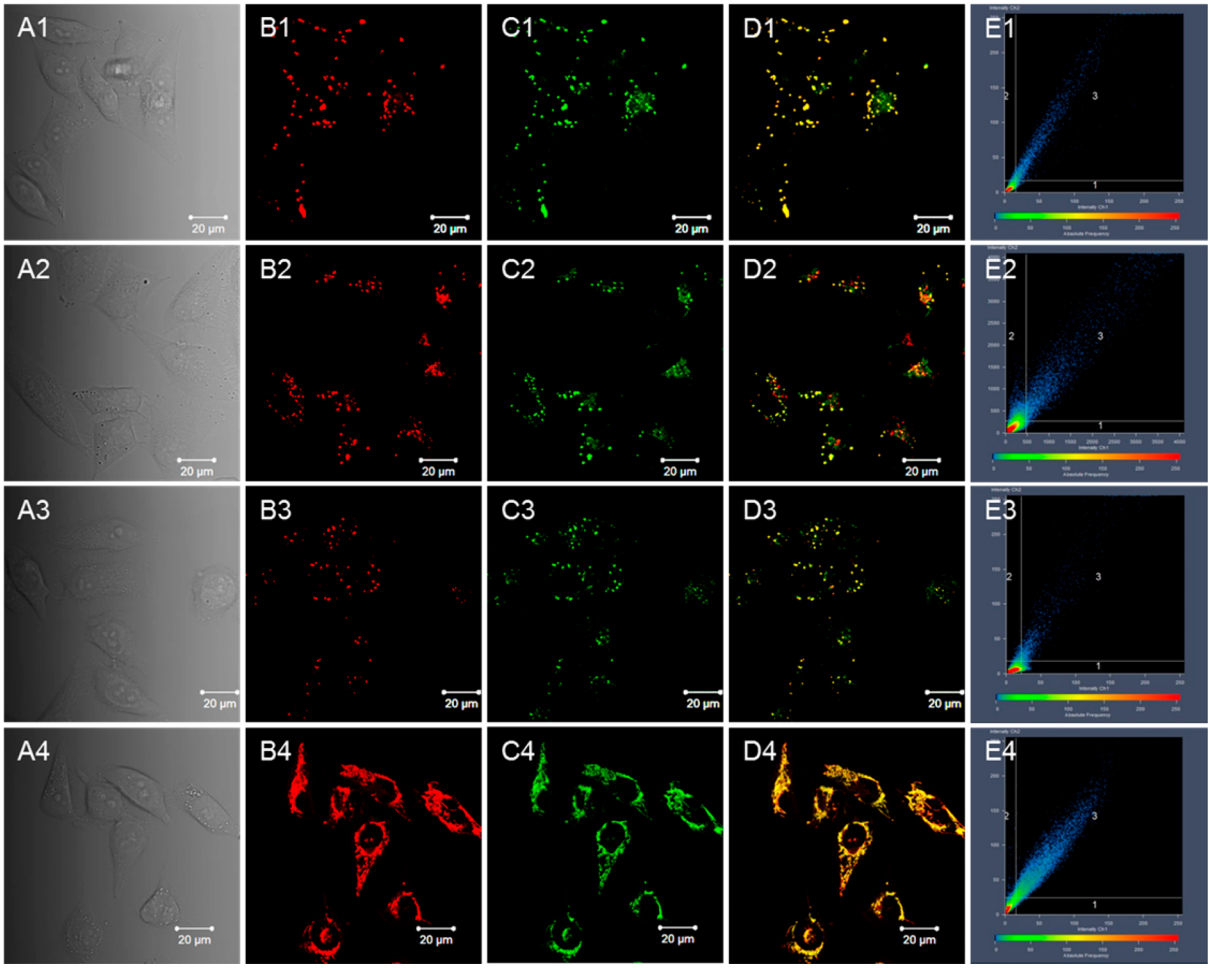

Figure 6. Co-localization imaging of HeLa cells stained with BODIPY 505/515 or MitoTracker Green FM and AIEgens. (A) Bright-field and (B, C) confocal images of HeLa cells stained with (B1) DCMa, (B2) DCIs, (B3) DCFu, (B4) DCPy, (C1−C3) BODIPY 505/515, and (C4) MitoTracker Green FM. (D1−D4) Merged images of panels B and C. (E1−E4) A scatter plot indicating a correction coefficient between panels B and C. λ_{ex}: 488 nm. Concentration: 5×10^{-7} M (DCMa, DCPy, MitoTracker Green FM, and BODIPY 505/515) and 2.5×10^{-6} M (DCIs and DCFu). Scale bar: 20 μm.

noted that there are two conformationally different molecules in the crystal structure of DCFu, and their main difference is the corresponding torsion angle, both of which are included in or out of parentheses (Figure 4).

As illustrated in Figure 4, the acceptor groups of DCMa, DCIs, DCFu, and DCPy reveal the small deviations from planarity of central carbazole manifested by the various small dihedral angles between acceptor and carbazole ring, suggesting well-conjugated systems. However, within each compound, the diphenylamino moiety adopts twisted conformations, and the twisted angles between the phenyl rings on N atom and the plane formed by N atom with three connected C atoms range from 28.98° to 58.99°. Besides, diphenylamino in four molecules is obviously twisted with respect to the central carbazole ring with dihedral angles vary from 26.98° to 47.50°. Structurally, strong push−pull character in combination with the extended π conjugation within fluorophores not only can effectively shift their emission wavelength to the far-red and NIR but also can dramatically improve their nonlinear optical properties, which are perfectly consistent with their far-red and NIR emission and excellent two-photon property. As a result, the presence of the twisted diphenylamino moiety effectively prevents the significant $\pi-\pi$ stacking between the molecules in the crystal packing and favors the AIE characteristic (Figure 5). Crystal packing diagrams of DCMa, DCIs, DCFu, and DCPy show that multiple inter- and intramolecular interactions such as C−H···π, C−H···N, C···π, and partial π···π interactions help rigidify the molecular conformation and lock the intramolecular rotations of the phenyl rings and the acceptor moiety against the central carbazole unit. Thus, the excited-state energy consumed by intramolecular rotation and TICT effect are greatly reduced in the solid state (powder, crystal, and aggregate), thus enabling the molecules to emit intense far-red and NIR fluorescence.

From the above, the designed AIEgens DCMa, DCIs, DCFu, and DCPy have been demonstrated to show the AIE characteristic with far-red and NIR emission, excellent two-photon absorption activity, and large Stokes shifts, all of which make them potential candidates for biological applications. Cytotoxicity is a potential side effect of the fluorophores that must be controlled when dealing with living cells, tissues, or animals. To meet the demand for further biological studies, the cytotoxicity of four AIEgens to living cells were initially evaluated by using 3-(4,5-dimethyl-2-thiazolyl)-2,5-diphenyltetrazolium bromide (MTT) assay at different concentrations for 24 h. As illustrated in Figure S31, no obvious decrease in cell viability is observed even at concentration of up to 5 μM, demonstrating the negligible cytotoxicity and superior bio-

DOI: 10.1021/acsnano.8b03138
ACS Nano 2018, 12, 8145−8159

compatibility of the four AIEgens to living cells at concentrations less than or equal to 5 μM.

Cell imaging experiments were further conducted by incubating HeLa cells with four AIEgens, namely DCMa, DCIs, DCFu, and DCPy, followed by the observation under a laser scanning confocal microscope under an excitation of 488 nm. As illustrated in Figure 6, the impressive bright fluorescence within HeLa cells can be observed from the red channel after incubation with AIEgens, suggesting a fast permeability of AIEgens for living cells. To realize the specificity of the AIEgens for cell imaging, the co-localization experiments was then carried out by incubating HeLa cells with each presented AIEgen and then BODIPY 505/515 or MitoTracker Green FM (Figure 6B,C), which are commercial probes for LDs and mitochondria imaging, respectively. It is interesting to find that DCMa, DCIs, and DCFu can stain LDs specifically suggested by the co-localization with BODIPY 505/515. Differently, DCPy specifically stains the mitochondria, as proven by the co-localization experiment with MitoTracker Green FM. For all of the AIEgens, the perfect overlapping of their images with that of BODIPY 505/515 or MitoTracker Green FM gives rise to high overlap coefficiencies (0.96−0.98) (Figure 6D,E), indicating their superior specificities for staining different organelles. The subcellular kinetic processes of DCMa and DCPy into HeLa cells were also studied as examples. As shown in Figures S32 and 33, DCMa could gradually visualize the LDs with a negligible background signal, which suggests that the excellent specificity of DCMa, DCIs, and DCFu to stain LDs can be attributed to the highly selective accumulation of the lipophilic AIEgens in the hydrophobic spherical LDs thanks to the "like−like" interactions. However, DCPy first stained the plasma membrane and then gradually transferred to light up the mitochondria with an increase of the incubation time. Different from the above three neutral AIEgens, the mitochondria-specific targeting capability of the cationic lipophilic DCPy mainly rely on the driven force of a very large membrane potential of around 180 mV across the mitochondrial membrane. Moreover, as shown in Figure 6, compared with the commercial probes, the images stained with AIEgens display a lower background signal mainly benefiting from their red-shifted emission. To further verify the organelle specificity of the AIEgens to normal cells, cell-imaging experiments using HEK 293T cells were performed under the same experiment conditions as those of HeLa cells. The results indicated that all AIEgens can stain HEK 293T cells efficiently (Figure S34), and the co-localization experiments further demonstrated the organelle specificity of DCMa, DCIs, and DCFu to LDs, and DCPy to mitochondria. These results revealed the good organelle specificity of the AIEgens to both normal cells and cancer cells. Generally, AIEgen may be uptaken by cells through endocytosis in aggregate form or may diffuse into cells in the isolated form. It is clear that even isolated AIEgen can specifically light up the organelles, and the fluorescence signal will become stronger and stronger upon aggregate formation by concentration accumulation. This normally will cause the ACQ effect if the traditional fluorophores are used. In addition, the presented AIEgens can be easily taken by the living cells without any further chemical modification or nanoparticle processing, which make them much simpler to use for organelle-specific staining.

Photostability, another key criteria for evaluating a fluorescent bioprobe, of these AIEgens was subsequently checked by continuous laser excitation and sequential scanning with a confocal microscope. As illustrated in Figure 7, for the AIEgens

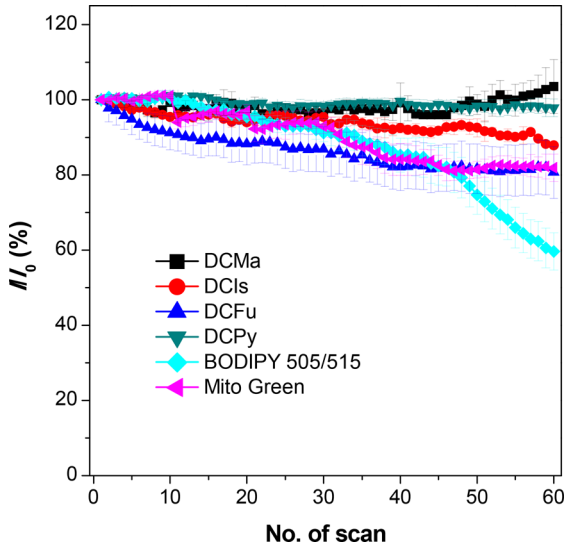

Figure 7. Loss in fluorescence of HeLa cells stained with AIEgens, MitoTracker Green FM, and BODIPY 505/515 with an increasing number of sequential scans of laser irradiation. Emission signal was normalized to the maximum intensity at the beginning of irradiation.

DCMa and DCPy, their fluorescence signals remain almost constant after 60 scans, whereas the fluorescence signals of DCIs and DCFu slightly decrease to 88% and 80% of its initial values. In comparison, for the commercial probes BODIPY 505/515 and MitoTracker Green FM, their fluorescence signals fade to 59% and 81%, respectively, of its initial values during the same process. That means, for the probe with the same specificity, the synthesized AIEgens display a superior photostability compared to the commercial dye.

Considering the excellent two-photon activity and high specificity of the developed AIEgens, the applicability for two-photon imaging of LDs and mitochondria were investigated for two representatives, namely DCMa and DCPy. As shown in Figure 8, DCMa and DCPy can clearly visualize the LDs and

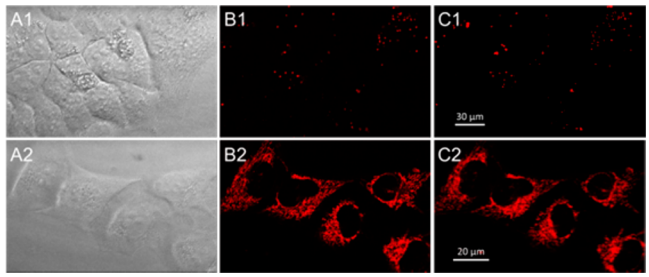

Figure 8. (A) Bright-field image of HeLa cells. One-photon excited images of HeLa cells stained with (B1) DCMa and (B2) DCPy. Two-photon excited images of HeLa cells stained with (C1) DCMa and (C2) DCPy in the same location. Concentration: 1 × 10^{-6} M (DCMa) and 5 × 10^{-7} M (DCPy).

mitochondria, respectively, within HeLa cells under two-photon excitation at 900 nm, revealing promising candidates as two-photon imaging probes for achieving NIR-to-NIR imaging of LDs or mitochondria in living cells.

Considering the excellent performance of the AIEgens at the cellular level, further investigations were carried out for staining the living tissues with more-complicated environments. Differ-

DOI: 10.1021/acsnano.8b03138
ACS Nano 2018, 12, 8145−8159

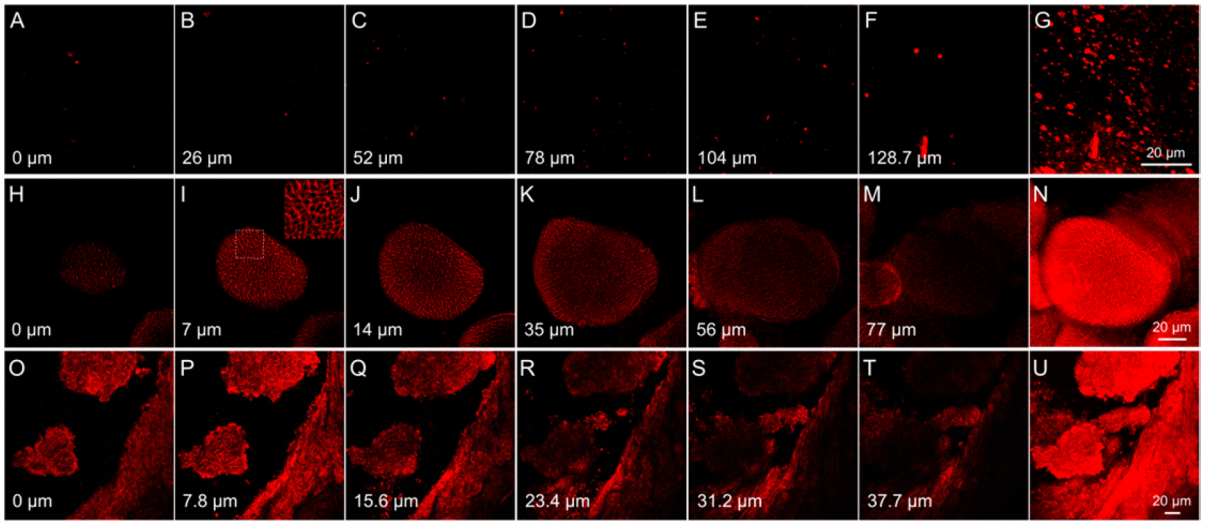

Figure 9. Two-photon fluorescent images of (A−F) a hepatic tissue stained with DCMa (5 μM), (H−M) muscle tissue stained with DCPy (5 μM), and (O−T) myocardial tissue stained with DCPy (5 μM) at different penetration depths. Z-projected image of (G) a hepatic tissue (z-stack of 100 slices, step size 1.3 of μm, and imaging depth of 128.7 mm), (N) a muscle tissue (z-stack of 80 slices, step size of 1.0 μm, and imaging depth of 80 mm), and (U) a myocardial tissue (z-stack of 30 slices, step size of 1.3 μm, and imaging depth of 38 mm). Two-photon excitation wavelength: 900 nm. Scale bar: 20 μm.

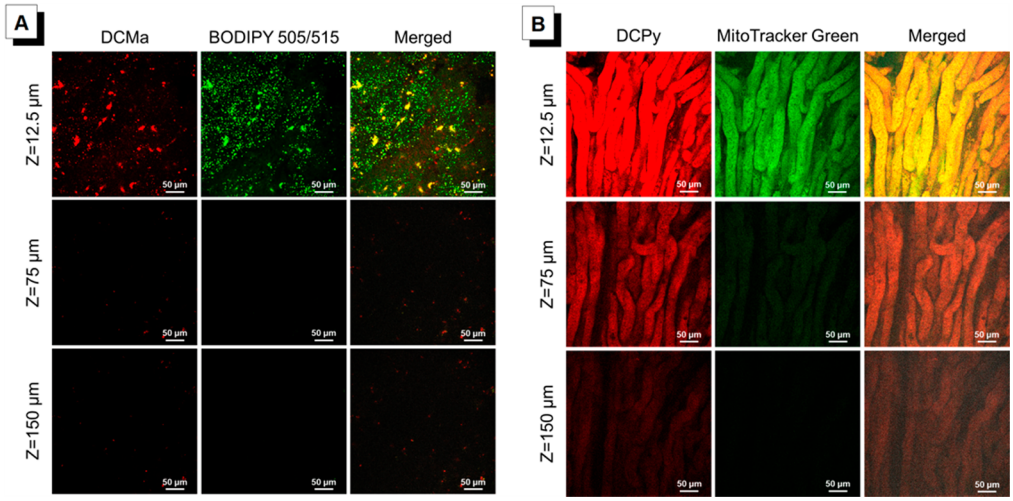

Figure 10. Two-photon microscopic images of (A) the excised hepatic tissue and (B) the excised nephric tissue of nude mouse after (A) DCMa and (B) DCPy injection in the tail vein for 2 h. Two-photon excitation wavelength: 900 nm. Scale bar: 50 μm.

ent from the microscopically imaging on the living cultured cells, *in situ* and directly imaging organelles, such as LDs and mitochondria, in intact tissues can offer more native and accurate information. It is well-known that the liver is the primary organ of lipid metabolism associated with various lipid-related physiological processes and the muscle is a tissue that is rich in mitochondria. In the following biological studies, the rat hepatic tissues, the rat skeletal muscle, and the rat myocardial tissue will be employed to evaluate the LD-specific imaging capability of DCMa and the mitochondria-specific imaging capability of DCPy at the tissue level, respectively. When a piece of hepatic tissue was stained with DCMa, as shown in Figure 9A−G, different sizes of the spherical LDs with intense red fluorescence could be clearly observed with almost no background under a two-photon microscope. Taking advantage of the two-photon excitation, Figure 9A−F show the images of the LDs at different depths with the maximum detectable depth up to around 129 μm, which is much deeper than the values obtained for the reported green AIEgen TPA-BI and other LDs probes.[66] The two-photon fluorescence imaging of the rat skeletal muscle stained by DCPy was also carried out and illustrated in Figure 9H−N. The imaging results indicate that DCPy can specifically stains mitochondria networks in rat skeletal muscle (Figure 9I inset), which is consistent with the previous reported studies for other dye.[68,76] Figure 9H−M show representative images of the mitochondria networks at different depths and mitochondria at a 77 μm depth can be still visualized by DCPy under two-photon excitation. This imaging depth is much improved compared to the very recently reported value of 50.9 μm for Mito-MOI.[76] In addition, the staining of myocardial tissue by DCPy was also studied, and panels O−U of Figure 9 show that mitochondria within myocardial tissue could be stained with a staining depth of 37.7 μm.[76]

Next, we investigated in a normal mouse model whether DCMa and DCPy are indeed able to stain LDs and mitochondria, respectively, *in vivo*. Considering that the

DOI: 10.1021/acsnano.8b03138
ACS Nano 2018, 12, 8145−8159

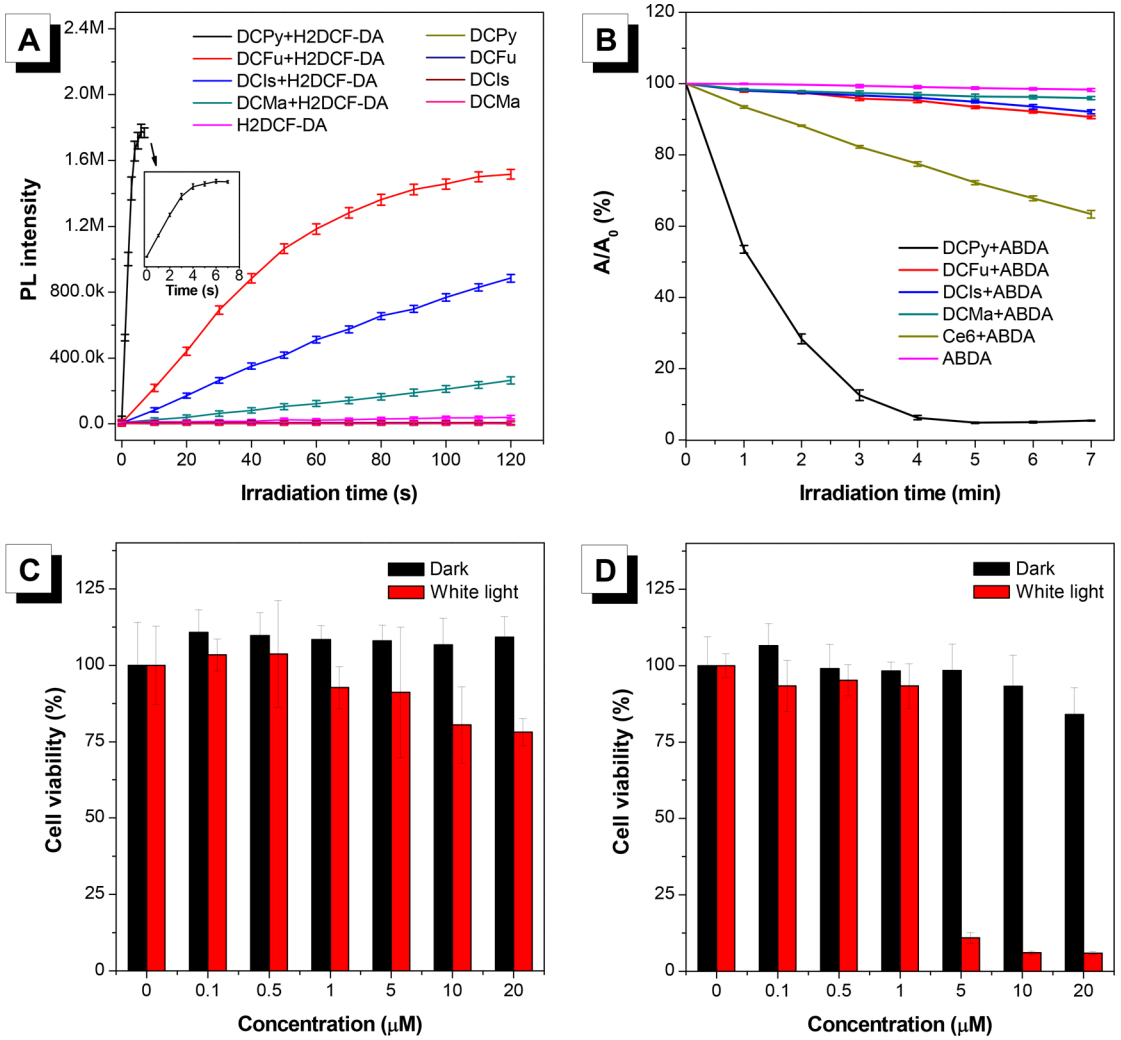

Figure 11. (A) Change of fluorescent intensity at 525 nm of H2DCF-DA in the presence or absence of DCMa, DCIs, DCFu, and DCPy in PBS upon white-light irradiation for different times. Concentration: 10×10^{-6} M (AIEgens) and 5×10^{-6} M (H2DCF-DA). (B) The decomposition rates of ABDA in the presence or absence of AIEgens and Ce6 under light irradiation, where A_0 and A are the absorbance of ABDA at 378 nm before and after irradiation, respectively. Concentration: 10×10^{-6} M (AIEgens) and 5×10^{-5} M (ABDA). Cell viability of HeLa cells stained with different concentrations of (C) DCFu or (D) DCPy under dark or under white-light irradiation.

nanoparticles with tens of nanometers tend to accumulate in internal organs during *in vivo* circulation,[77] the main organs of nude mouse were resected at 2 h after AIEgen (DCMa or DCPy) injection in the tail vein. *Ex vivo* fluorescence imaging of the resected major organs revealed that the DCMa nanoaggregates were mainly localized in the liver and lung (Figure S35), whereas the DCPy nanoaggregates tend to accumulate in the liver and kidney tissue. In spite of their distinct organs distributions, the organelle-targeting specificity of the intravenously injected DCMa or DCPy in the representative hepatic tissue or nephric tissue was examined under two-photon excited fluorescence microscopy. As shown in Figure 10A, very bright dot-like fluorescent signal was observed under 900 nm two-photon excitation, and further co-localization with BODIPY 505/515 indicated the good specificity of DCMa to LDs although not all of the LDs were stained, probably because of the poor circulation of the dye in the small capillaries of hepatic tissue. However, DCPy can clearly visualize the nephric tissue (Figure 10B). Its nice co-localization with MitoTracker Green FM revealed its good specificity to mitochondria *in vivo*. Notably, deep hepatic tissue or nephric tissue imaging at a depth of up to 150 μm can be still visualized by DCMa or DCPy. In contrast, the fluorescent signal of commercial probes was not detected under the same circumstances. Clearly, the presented AIEgens exhibit superiority compared with commercial probes in terms of deeper penetration. These above results reveal that, upon two-photon excitation, DCMa and DCPy can effectively stain LDs and mitochondria, respectively, in both living cells and tissues with no background and high penetration depth thanks to the combination of the two-photon NIR excitation and far-red and NIR emission properties of AIEgens. These results also reveal the great potential of these AIEgens serve as one- and two-photon bioprobes for studying LDs- or mitochondria-related biological processes in cells, tissues, and mouse models.

More interestingly, these AIEgens not only possess specific imaging functionality but also can efficiently generate reactive oxygen species (ROS) upon light irradiation for photodynamic therapy (PDT). Because all the AIEgens have strong absorption in the visible light region, their ROS generation was evaluated under white light irradiation using a commercial ROS indicator H2DCF-DA, which is capable of emitting fluorescence at around 525 nm when oxidized by ROS. As shown in Figure 11A,

DOI: 10.1021/acsnano.8b03138
ACS Nano 2018, 12, 8145–8159

for the mixture of each AIEgen and H2DCF-DA in phosphate-buffered saline (PBS) buffer, the green fluorescence generated by the oxidized indicator was gradually intensified with increasing irradiation time. Such a change, however, was not observed for each AIEgen or H2DCF-DA alone under the same conditions. Figure 11A suggests that four AIEgens exhibit the different ROS generation efficiency in the order of DCPy > DCFu > DCIs > DCMa. In particular, in the presence of cationic DCPy, the fluorescence of the indicator reaches the maximum plateau within only 6 s, indicating an extremely high ROS-generation efficiency. Notably, among the various kinds of ROS including singlet oxygen ($^1O_2$), superoxide radicals ($O_2^{\bullet-}$), hydrogen peroxide (H_2O_2), and hydroxyl radicals (•OH), $^1O_2$ is regarded as a primary cytotoxic agent for triggering cell death involved in the photodynamic process.[78−80] Thus, the efficient $^1O_2$ generation of these AIEgens is desirable for realizing satisfied PDT. We therefore assess the capability of these AIEgens for $^1O_2$ generation using 9,10-anthracenediyl-bis-(methylene)-dimalonic acid (ABDA), which could undergo oxidation by $^1O_2$ to yield endoperoxide, resulting in a decrease of ABDA absorption. Under white light irradiation, as shown in Figure 11B, the absorbance of ABDA solution in the presence of DCMa, DCIs, or DCFu decreases gradually with prolonged irradiation time, whereas a prodigious drop of ABDA absorption was observed for DCPy. As depicted in Figure S36, from the changes of the ABDA absorbance in the presence of each AIEgens, the decomposition rate of ABDA was calculated to be 0.49, 0.85, 1.26, and 11.13 nmol min^{-1} for DCMa, DCIs, DCFu, and DCPy, respectively. For comparison, a value of 4.21 nmol min^{-1} was obtained for Ce6, which is the most widely used photosensitizer in image-guided PDT.[81,82] These results clearly suggest that DCPy could generate $^1O_2$ more effectively compared to Ce6; meanwhile, AIEgens DCMa, DCIs, and DCFu could be served as moderate photosensitizers. The potential photothermal effect of AIEgens was excluded by the negligible temperature change of AIEgen suspension at different concentrations (5−30 μM) as a function of white-light irradiation time (Figure S37).

These interesting findings motivated us to further investigate their performance as photosensitizers for PDT on living cells. We initially evaluated the white-light irradiation triggered ROS generation of DCPy inside HeLa cells through incubation either with both H2DCF-DA and DCPy or with H2DCF-DA alone. As shown in Figure S38, an obvious increase in the fluorescence signal was observed from the cells incubated with both H2DCF-DA and DCPy with increasing irradiation time, revealing efficient ROS generation from DCPy under white-light irradiation. In contrast, no obvious fluorescence increase was observed in the absence of DCPy. Then quantitative evaluation of the therapeutic effect was studied by the standard MTT assay employing HeLa cells as a model (Figure 11C,D). Upon incubation of HeLa cells with DCFu and DCPy for 24 h under dark conditions, the cell viability was still higher than 100% (DCFu) and 84% (DCPy) no matter the concentration of AIEgens used (up to 20 μM), suggesting low cytotoxicity of these AIEgens in dark conditions. However, with the white-light irradiation, a dose-dependent toxicity is observed for DCFu and DCPy. DCFu displays the moderate cytotoxicity reflected by the gradual decrease of cell viability down to 78% at a concentration of 20×10^{-6} M. As for DCPy, cell viability shows no obvious change at the concentration below 1×10^{-6} M, whereas a sharp drop to 10% was found at a higher concentration of 5×10^{-6} M. In contrast, for the commercial Ce6, cell viability shows remarkable decline from 80% to 10% at the concentration of 20×10^{-6} M (Figure S39). These results demonstrate that the synthesized AIEgens DCFu and DCPy are promising in killing cancer cells through photodynamic processes. In particular, DCPy was proven to be much more efficient than Ce6, which is in line with the outcomes of $^1O_2$ generation. As mentioned previously, it would be ideal for efficient photodynamic applications if the photosensitizer can be localized at mitochondria and subsequently cause damage *in situ* by the generated $^1O_2$ with light irradiation. Obviously, DCPy is the case possessing both high $^1O_2$ generation and mitochondria-specific targeting capability, both of which were recently realized by a much more complicated protein−ruthenium complex.[63] Overall, as described for DCFu and, in particular, DCPy, they all cause less damage to living cells at low concentrations, even with long light irradiation, making them ideal candidates for promising applications with dual functionalities of cell imaging and therapy modulated by AIEgen concentrations.

CONCLUSIONS

In summary, a family of far-red and NIR fluorophores based on a carbazole-bridged push−pull framework is well-synthesized and -characterized. Far-red and NIR emission of fluorophores is successfully achieved when different strong electron acceptors (malononitrile, isophorone, methylpyridinium salt, and 3-cyano-4-phenyl-2(5H)-furanone) are conjugated to the strong electron-donating diphenylamino through ingenious molecular engineering. These luminogenic molecules show significant solvatochromism in solvents with different polarities; meanwhile, the typical TICT effect observed for fluorophores in polar solvent such as DMSO results in their fluorescence quenching. The two-photon excited fluorescence measurements reveal that these fluorophores display excellent two-photon absorption cross-sections (σ_{2P} maximum: 390−887 GM) in the range of 800−1040 nm. Further study demonstrates that all of the compounds show typical AIE characteristics, with the emission maximum ranging from 665 to 755 nm thanks to their twisted and rotatable molecular structures suggested by the crystallographic analysis. Impressively, fluorophores DCMa, DCIs, and DCFu can specifically stain LDs, while the cationic lipophilic DCPy shows superior mitochondria-specific targeting capability. For cell imaging, all these AIEgens display good biocompatibility and high contrast as well as higher photostability than the commercial probes. Furthermore, under two-photon microscopy, DCMa and DCPy can efficiently label LDs and mitochondria in living cells and living tissues with deep tissue penetration (up to 150 μm) and high contrast. Moreover, under white-light irradiation, efficient $^1O_2$ generation of these fluorophores (particularly DCPy) enables the effective application for photodynamic killing of cancer cells, revealing the great potential of these AIEgens served as one- and two-photon bioprobes for LD- or mitochondria-targeted and image-guided photodynamic cancer therapy. This study not only provides an ideal AIE platform combining efficient far-red and NIR emission, excellent two-photon absorption properties, LD- or mitochondria-specific staining capability, and therapeutic effect but also could intrigue the development of two-photon absorbing far-red and NIR AIEgens for organelle-targeted therapeutic applications.

EXPERIMENTAL SECTION

Chemicals and Methods. All chemicals and reagents were commercially available and used as received without further

DOI: 10.1021/acsnano.8b03138
ACS Nano 2018, 12, 8145−8159

purification. The intermediates 2,7-dibromo-9-ethyl-9*H*-carbazole, 1,4-dimethylpyridinium iodide, and 3-cyano-4-phenyl-2(5H)-furanone were synthesized refer to the reported procedures.[83−85] 2′,7′-Dichlorodihydrofluorescein diacetate (H2DCF-DA), 9,10-anthracene-diyl-bis(methylene)dimalonic acid (ABDA), and 3-(4,5-dimethyl-2-thiazolyl)-2,5-diphenyltetrazolium bromide (MTT) were purchased from Sigma-Aldrich and used as received. For cell culture, minimum essential medium (MEM), fetal bovine serum (FBS), penicillin−streptomycin solution, BODIPY 505/515, and MitoTracker Green FM were purchased from Invitrogen. ^{1}H and ^{13}C NMR spectra were measured on a Bruker ARX 400 NMR spectrometer using $CDCl_3$ and DMSO-d_6 as solvents, and tetramethylsilane (TMS; δ = 0 ppm) was chosen as the internal reference. High-resolution mass spectra (HRMS) were obtained on a Finnigan MAT TSQ 7000 mass spectrometer system operated in a matrix-assisted laser desorption and ionization−time-of-flight (MALDI-TOF) mode. Absorption spectra were measured on a Milton Roy Spectronic 3000 array spectrophotometer. Steady-state photoluminescence (PL) spectra were measured on a PerkinElmer spectrofluorometer LS 55. Absolute fluorescence quantum yield was measured by a calibrated integrating sphere (Labsphere). Single-crystal data were collected on a Bruker Smart APEXII charge-coupled device (CCD) diffractometer using graphite monochromated Cu Kα radiation (λ = 1.54178 Å). Particle-size analysis was determined at room temperature using a Zetaplus potential analyzer (Brookhaven Instruments Corporation). A two-photon excitation fluorescence cross-section was measured by two-photon excitation fluorescence method using rhodamine B as a reference. The excitation source for two-photon excitation was a femtosecond optical parametric amplifier (Coherent OPerA Solo) pumped by an amplified Ti:sapphire system (Coherent Legend Elite system) and then detected with a spectrometer (Acton SpectraPro-500i) coupled to a CCD. Simulation was carried out with the Gaussian 09 package. Fluorescence images were collected on an Olympus BX 41 fluorescence microscope. Laser confocal scanning microscope images were collected on a Zeiss laser scanning confocal microscope (LSM710) and analyzed using ZEN 2009 software (Carl Zeiss).

Synthesis of DCMa. 7-(Diphenylamino)-9-ethyl-9H-carbazole-2-carbaldehyde (0.39 g, 1.0 mmol) and malononitrile (0.08 g, 1.2 mmol) were dissolved in ethanol (5 mL) and refluxed for 4 h. Upon cooling to room temperature, the reaction mixture produced a red powder that was filtered, washed by cold ethanol, and dried under a vacuum. The crude product was further purified by recrystallization from acetonitrile, giving DCMa as a red crystalline solid (0.37 g, yield: 85%) with a melting point of 196−198 °C. ^{1}H NMR (400 MHz, $CDCl_3$, ppm, δ): 8.07 (s, 1H), 8.04 (d, J = 8.2, 1H), 7.94 (d, J = 8.6, 1H), 7.89 (s, 1H), 7.62 (dd, J = 8.2 Hz, 1.4 Hz, 1H), 7.33−7.29 (m, 4H), 7.19−7.18 (m, 4H), 7.12−7.08 (m, 2H), 7.06 (d, J = 1.7, 1H), 7.01 (dd, J = 8.6 Hz, 1.9 Hz, 1H), 4.22 (q, J = 7.2, 2H), 1.37 (t, J = 7.2, 3H). ^{13}C NMR (100 MHz, $CDCl_3$, ppm, δ): 159.92, 148.58, 147.01, 143.01, 139.22, 128.80, 128.24, 126.21, 124.31, 122.96, 122.64, 121.63, 119.43, 116.48, 116.27, 114.15, 113.32, 109.29, 102.01, 77.91, 37.09, 13.09. HRMS (MALDI-TOF) (m/z): $[M]^+$ calcd for $C_{30}H_{22}N_4$, 438.1844; found, 438.1860.

Synthesis of DCIs. 7-(Diphenylamino)-9-ethyl-9H-carbazole-2-carbaldehyde (0.39 g, 1.0 mmol) and 2-(3,5,5-trimethylcyclohex-2-enylidene)-malononitrile (0.2 g, 1.1 mmol) were dissolved in dry acetonitrile (8 mL). A single drop of piperidine was added, and the solution was refluxed overnight. After the reaction mixture was cooled, the red solid was filtered, washed with acetonitrile, and dried to give DCIs as a red crystalline solid (0.42 g, yield: 75%) with a melting point of 255−258 °C. ^{1}H NMR (400 MHz, $CDCl_3$, ppm, δ): 7.97 (d, J = 8.1 Hz, 1H), 7.91 (d, J = 8.4 Hz, 1H), 7.49 (s, 1H), 7.37 (d, J = 8.1 Hz, 1H), 7.29−7.25 (m, 5H), 7.17−7.09 (m, 6H), 7.05−7.02 (m, 2H), 6.97 (dd, J = 8.5 Hz, 1.8 Hz, 1H), 6.89 (s, 1H), 4.23 (q, J = 7.2 Hz, 2H), 2.62 (s, 2H), 2.53 (s, 2H), 1.36 (t, J = 7.2 Hz, 3H), 1.10 (s, 6H). ^{13}C NMR (100 MHz, $CDCl_3$, ppm, δ): 168.66, 153.74, 147.43, 146.67, 141.58, 140.00, 137.99, 131.66, 128.62, 127.28, 124.21, 123.60, 122.38, 122.19, 120.71, 119.53, 118.91, 117.51, 116.67, 113.13, 112.44, 106.41, 103.41, 77.04, 42.36, 38.63, 36.84, 31.46, 27.44, 13.20. HRMS (MALDI-TOF) (m/z): $[M]^+$ calcd for $C_{39}H_{34}N_4$, 558.2783; found, 558.2764.

Synthesis of DCFu. 7-(Diphenylamino)-9-ethyl-9H-carbazole-2-carbaldehyde (0.38 g, 0.97 mmol) and 3-cyano-4-phenyl-2(5H)-furanone (0.18 g, 0.97 mmol) were dissolved in ethanol (13 mL) and refluxed overnight. Upon cooling to room temperature, the reaction mixture produced a violet powder that was filtered, washed by cold ethanol, and dried under a vacuum. The crude product was further purified by flash silica gel column chromatography eluting with dichloromethane, giving DCFu as a violet crystalline solid (0.46 g, yield: 85%) with a melting point of 256−258 °C. ^{1}H NMR (400 MHz, $CDCl_3$, ppm, δ): 7.98 (d, J = 8.2 Hz, 1H), 7.96 (s, 1H), 7.91 (d, J = 8.5 Hz, 1H), 7.69−7.61 (m, 5H), 7.59 (dd, J = 8.2 Hz, 1.2 Hz, 1H), 7.30−7.26 (m, 4H), 7.18−7.16 (m, 4H), 7.08−7.04 (m, 3H), 6.98 (dd, J = 8.5 Hz, 1.8 Hz, 1H), 6.66 (s, 1H), 4.24 (q, J = 7.2 Hz, 2H), 1.35 (t, J = 7.2 Hz, 3H). ^{13}C NMR (100 MHz, $CDCl_3$, ppm, δ): 163.88, 163.19, 147.62, 147.22, 144.23, 142.32, 139.81, 131.49, 128.93, 128.70, 128.40, 127.64, 127.28, 125.48, 123.96, 123.47, 122.92, 122.56, 121.19, 119.40, 116.89, 116.52, 111.43, 110.97, 102.75, 96.86, 36.90, 13.18. HRMS (MALDI-TOF (m/z) $[M]^+$: calcd for $C_{38}H_{27}N_3O_2$, 557.2103; found, 557.2127.

Synthesis of DCPy. 7-(Diphenylamino)-9-ethyl-9H-carbazole-2-carbaldehyde (0.5 g, 1.28 mmol) and 1,4-dimethylpyridinium iodide (0.27 g, 1.16 mmol) were dissolved in dry ethanol (15 mL). A single drop of piperidine was added, and the solution was refluxed for 3 h. Upon cooling to room temperature, the red precipitated solid was filtered, washed with cold ethanol, and dried to give the iodide salt of the product as a red solid (0.56 g, yield: 80%). Next, the solid was dissolved in acetone (20 mL), and a saturated aqueous solution of KPF_6 (20 mL) was then added. After 30 min of stirring, the solution was evaporated to dryness. The residue was purified by flash silica gel column chromatography eluted with dichloromethane and methanol (20:1, v/v), giving DCPy as a red crystalline solid (0.57 g, yield: 99%) with a melting point of 321−322 °C. ^{1}H NMR (400 MHz, DMSO-d_6, ppm, δ): 8.81 (d, J = 6.7 Hz, 2H), 8.19−8.11 (m, 4H), 8.07 (d, J = 8.4 Hz, 1H), 7.93 (s, 1H), 7.62−7.56 (m, 2H), 7.31−7.28 (m, 4H), 7.18 (s, 1H), 7.06−7.01 (m, 6H), 6.86 (dd, J = 8.4 Hz, 1.7 Hz, 1H), 4.30 (q, J = 6.9 Hz, 2H), 4.22 (s, 3H), 1.23 (t, J = 7.1 Hz, 3H). ^{13}C NMR (100 MHz, DMSO-d_6, ppm, δ): 152.58, 147.36, 146.49, 144.77, 141.95, 141.59, 140.00, 131.75, 129.32, 124.10, 123.50, 122.94, 122.73, 121.79, 121.71, 120.09, 119.50, 117.61, 116.77, 108.58, 104.18, 46.60, 36.80, 13.45. HRMS (MALDI-TOF (m/z): $[M]^+$ calcd for $C_{34}H_{30}F_6N_3P$, 625.2082; found, 625.2060.

Cell Culture. HeLa cells were cultured in MEM containing 10% FBS and antibiotics (100 units per milliliter of penicillin and 100 μg/mL streptomycin) in a 5% CO_2 humidity incubator at 37 °C.

Cytotoxicity Study. Cytotoxicity was evaluated by the 3-(4,5-dimethythiazol-2-yl)-2,5-diphenyltetrazolium bromide (MTT) assays in accordance to the manufacturer's manual. Cells were seeded in 96-well plates at a density of about 10 000 cells per well. After 24 h of culturing, the medium in each well was replaced by 100 μL of fresh medium containing different concentrations (0, 0.1, 0.5, 1, and 5 μM) of certain dyes (DCMa, DCIs, DcFu, and DCPy). The volume fraction of DMSO was below 0.2%. After 24 h, 10 μL of MTT solution (5 mg/mL in PBS) was added into each well. After 4 h of incubation, DMSO was added into each well, and the plate was gently shaken to dissolve all of the precipitated formed. Finally, the absorption of each well at 570 nm was recorded via a plate reader (PerkinElmer Victor3TM). Each trial was performed with five parallel wells.

Cytotoxicity of DCFu and DCPy to Cancer Cells under Light Irradiation. HeLa cells were seeded in 96-well plates (Costar, IL) at a density of 6000−8000 cells per well. After overnight culturing, medium in each well was replaced by 100 μL of fresh medium containing different concentrations of DCFu or DCPy. The volume fraction of DMSO is below 0.2%. After incubation for 30 min, plates containing HeLa cells with fresh medium were exposed to white light (4.2 mW/cm^{-2}) for 90 min, and another array of plates with cells was kept in the dark as a control. Then, the plates were given the same treatment as the biocompatibility test.

Cell Imaging. HeLa cells were grown in a 35 mm Petri dish with a coverslip. The cells were stained with certain dye at certain concentration (by adding 2 μL of 2 mM certain dyes in DMSO to 2

DOI: 10.1021/acsnano.8b03138
ACS Nano 2018, 12, 8145−8159

mL of MEM with DMSO, <0.1 vol %) for 30 min followed by MitoTracker Green (0.5 μM) or BODIPY 505/515 (0.5 μM) for a specific time. The cells were imaged under a confocal microscope (Zeiss LSM 710 laser scanning confocal microscope) using proper excitation and emission filters for each dye: for DCMa, DCIs, DcFu, and DCPy, the excitation filter was 488 nm and the emission filter 600−700 nm; for BODIPY 505/515 and MitoTracker Green, the excitation filter was 488 nm and the emission filter 500−530 nm.

Photostability. The Hela Cells labeled with certain dyes were imaged by a confocal microscope (Zeiss LSM 710 laser scanning confocal microscope), and the dyes were excited with a 488 nm laser light for one-photon imaging. Imaging parameters were set for each dye individually to obtain optimal images. Continuous scans (11 s per scan) were taken. On each series of scans, three regions of interest (ROIs) with mitochondria and lipid droplets were defined. The first scan of each ROI was set to 100%. Next, the pixel intensity values for each ROI were averaged and plotted against the scan number. The resulting curve represented the bleaching rate that an experimentalist would encounter.

Two-Photon Fluorescence Imaging in Cells and Tissues. HeLa cells used for two-photon microscopy were stained with DCMa (1.0 μM) or DCPy (0.5 μM) refer to the procedure described for confocal fluorescence imaging. The rat skeletal muscle, cardiac muscle, and hepatic tissues were directly removed from just-sacrificed adult Wistar rats. Next, they were stained with DCMa (5.0 μM) or DCPy (1.0 μM) for 30 min at room temperature in H-Dulbecco's modified Eagle medium supplemented with 10% fetal bovine serum and 1% penicillin and streptomycin. The two-photon fluorescence images of HeLa cells and the rat skeletal muscle, cardiac muscle, and hepatic tissues debris were collected using a stimulated emission depletion microscopy (Leica Stimulated Emission Depletion Microscope) equipped with a multiphoton laser (Coherent Chameleon Ultra II Multiphoton laser) with an excitation wavelength of 900 nm and an emission filter of 600−700 nm.

ROS-Generation Detection. H2DCF-DA was used as the ROS-monitoring agent. In the experiments, 10 μL of H2DCF-DA stock solution (1.0 mM) was added to 2 mL of AIEgen suspension (10 μM), and white light (4.2 mW/cm^{-2}) was employed as the irradiation source. The emission of H2DCF-DA at 525 nm was recorded at various irradiation times.

$^1O_2$-Generation Detection. ABDA was used as the $^1O_2$-monitoring agent. In the experiments, 13 μL of ABDA stock solution (7.5 mM) was added to 2 mL of AIEgen suspension (10 μM), and white light (4.2 mW/cm^{-2}) was employed as the irradiation source. The absorption of ABDA at 378 nm was recorded at various irradiation times to obtain the decay rate of the photosensitizing process.

ASSOCIATED CONTENT

Supporting Information

The Supporting Information is available free of charge on the ACS Publications website at DOI: 10.1021/acsnano.8b03138.

Additional details on the syntheses and characterizations (^{1}H NMR, ^{13}C NMR, and HRMS) of the intermediates and final compounds and the spectral data. (PDF)
X-ray crystallographic data (CIF)
X-ray crystallographic data (CIF)
X-ray crystallographic data (CIF)
X-ray crystallographic data (CIF)

AUTHOR INFORMATION

Corresponding Author

*E-mail: tangbenz@ust.hk.

ORCID

Zheng Zheng: 0000-0001-9312-6582
Ryan T. K. Kwok: 0000-0002-6866-3877
Ben Zhong Tang: 0000-0002-0293-964X

Author Contributions

⊥Z. Z., T. Z., and H. L. contributed equally to this work.

Notes

The authors declare no competing financial interest.

ACKNOWLEDGMENTS

We are grateful for financial support from the National Science Foundation of China (21788102), the Research Grants Council of Hong Kong (16308016, C2014-15G, C6009-17G, AoE/P-02/12 and A-HKUST605/16), the Innovation and Technology Commission (ITC−CNERC14SC01) and the Science and Technology Plan of Shenzhen (JCYJ20160229205601482 and JCYJ20140425170011516).

REFERENCES

(1) Weissleder, R.; Pittet, M. J. Imaging in the Era of Molecular Oncology. *Nature* **2008**, *452*, 580−589.
(2) Xie, J.; Liu, G.; Eden, H. S.; Ai, H.; Chen, X. Surface-Engineered Magnetic Nanoparticle Platforms for Cancer Imaging and Therapy. *Acc. Chem. Res.* **2011**, *44*, 883−892.
(3) Chen, G.; Roy, I.; Yang, C.; Prasad, P. N. Nanochemistry and Nanomedicine for Nanoparticle-Based Diagnostics and Therapy. *Chem. Rev.* **2016**, *116*, 2826−2885.
(4) Weissleder, R. A Clearer Vision for *in Vivo* Imaging. *Nat. Biotechnol.* **2001**, *19*, 316−317.
(5) Michalet, X.; Pinaud, F.; Bentolila, L.; Tsay, J.; Doose, S.; Li, J.; Sundaresan, G.; Wu, A.; Gambhir, S.; Weiss, S. Quantum Dots for Live Cells, *in Vivo* Imaging, and Diagnostics. *Science* **2005**, *307*, 538−544.
(6) Chan, J.; Dodani, S. C.; Chang, C. J. Reaction-Based Small-Molecule Fluorescent Probes for Chemoselective Bioimaging. *Nat. Chem.* **2012**, *4*, 973−984.
(7) Smith, A. M.; Mancini, M. C.; Nie, S. Bioimaging: Second Window for *in Vivo* Imaging. *Nat. Nanotechnol.* **2009**, *4*, 710−711.
(8) Yin, J.; Hu, Y.; Yoon, J. Fluorescent Probes and Bioimaging: Alkali Metals, Alkaline Earth Metals and pH. *Chem. Soc. Rev.* **2015**, *44*, 4619−4644.
(9) Yang, Y.; Zhao, Q.; Feng, W.; Li, F. Luminescent Chemodosimeters for Bioimaging. *Chem. Rev.* **2013**, *113*, 192−270.
(10) Escobedo, J. O.; Rusin, O.; Lim, S.; Strongin, R. M. NIR Dyes for Bioimaging Applications. *Curr. Opin. Chem. Biol.* **2010**, *14*, 64−70.
(11) Yuan, L.; Lin, W.; Zheng, K.; He, L.; Huang, W. Far-Red to Near Infrared Analyte-Responsive Fluorescent Probes Based on Organic Fluorophore Platforms for Fluorescence Imaging. *Chem. Soc. Rev.* **2013**, *42*, 622−661.
(12) Guo, Z.; Park, S.; Yoon, J.; Shin, I. Recent Progress in the Development of Near-Infrared Fluorescent Probes for Bioimaging Applications. *Chem. Soc. Rev.* **2014**, *43*, 16−29.
(13) Shanmugam, V.; Selvakumar, S.; Yeh, C. S. Near-Infrared Light-Responsive Nanomaterials in Cancer Therapeutics. *Chem. Soc. Rev.* **2014**, *43*, 6254−6287.
(14) Zhang, X.; Wang, C.; Han, Z.; Xiao, Y. A Photostable Near-Infrared Fluorescent Tracker with pH-Independent Specificity to Lysosomes for Long Time and Multicolor Imaging. *ACS Appl. Mater. Interfaces* **2014**, *6*, 21669−21676.
(15) Liu, W.; Wang, Y.; Han, X.; Lu, P.; Zhu, L.; Sun, C.; Qian, J.; He, S. Fluorescence Resonance Energy Transfer (FRET) Based Nanoparticles Composed of AIE Luminogens and NIR Dyes with Enhanced Three-Photon Near-Infrared Emission for *in Vivo* Brain Angiography. *Nanoscale* **2018**, *10*, 10025−10032.
(16) Lv, Y.; Liu, M.; Zhang, Y.; Wang, X.; Zhang, F.; Li, F.; Bao, W.; Wang, J.; Zhang, Y.; Wei, W.; et al. Cancer Cell Membrane-Biomimetic Nanoprobes with Two-Photon Excitation and Near-Infrared Emission for Intravital Tumor Fluorescence Imaging. *ACS Nano* **2018**, *12*, 1350−1358.
(17) Zhang, X.; Bloch, S.; Akers, W.; Achilefu, S. Near-Infrared Molecular Probes for *in Vivo* Imaging. *Curr. Protoc. Cytom.* **2012**, *12*, 12271−122720.
(18) Luo, S.; Zhang, E.; Su, Y.; Cheng, T.; Shi, C. A Review of NIR Dyes in Cancer Targeting and Imaging. *Biomaterials* **2011**, *32*, 7127−7138.

DOI: 10.1021/acsnano.8b03138
ACS Nano 2018, 12, 8145−8159

(19) Frangioni, J. *In Vivo* Near-Infrared Fluorescence Imaging. *Curr. Opin. Chem. Biol.* **2003**, *7*, 626−634.
(20) Birks, J. B. *Photophysics of Aromatic Molecules*, Wily-Interscience: London, England, 1970; pp 528−537.
(21) Luo, J.; Xie, Z.; Lam, J. W.; Cheng, L.; Chen, H.; Qiu, C.; Kwok, H. S.; Zhan, X.; Liu, Y.; Zhu, D.; et al. Aggregation-Induced Emission of 1-methyl-1, 2, 3, 4, 5-pentaphenylsilole. *Chem. Commun.* **2001**, 1740−1741.
(22) Yu, Z.; Duan, Y.; Cheng, L.; Han, Z.; Zheng, Z.; Zhou, H.; Wu, J.; Tian, Y. Aggregation Induced Emission in the Rotatable Molecules: the Essential Role of Molecular Interaction. *J. Mater. Chem.* **2012**, *22*, 16927−16932.
(23) Wang, L.; Shen, Y.; Yang, M.; Zhang, X.; Xu, W.; Zhu, Q.; Wu, J.; Tian, Y.; Zhou, H. Novel Highly Emissive H-Aggregates with Aggregate Fluorescence Change in a Phenylbenzoxazole-Based System. *Chem. Commun.* **2014**, *50*, 8723−8726.
(24) Mei, J.; Leung, N. L.; Kwok, R. T.; Lam, J. W.; Tang, B. Z. Aggregation-Induced Emission: Together We Shine, United We Soar! *Chem. Rev.* **2015**, *115*, 11718−11940.
(25) Zhang, J.; Ma, S.; Fang, H.; Xu, B.; Sun, H.; Chan, I.; Tian, W. Insights into the Origin of Aggregation Enhanced Emission of 9, 10-Distyrylanthracene Derivatives. *Mater. Chem. Front.* **2017**, *1*, 1422−1429.
(26) Qin, W.; Ding, D.; Liu, J.; Yuan, W. Z.; Hu, Y.; Liu, B.; Tang, B. Z. Biocompatible Nanoparticles with Aggregation-Induced Emission Characteristics as Far-Red/Near-Infrared Fluorescent Bioprobes for *in Vitro* and *in Vivo* Imaging Applications. *Adv. Funct. Mater.* **2012**, *22*, 771−779.
(27) Qin, W.; Li, K.; Feng, G.; Li, M.; Yang, Z.; Liu, B.; Tang, B. Z. Bright and Photostable Organic Fluorescent Dots with Aggregation-Induced Emission Characteristics for Noninvasive Long-Term Cell Imaging. *Adv. Funct. Mater.* **2014**, *24*, 635−643.
(28) Kang, M.; Gu, X.; Kwok, R. T.; Leung, C. W.; Lam, J. W.; Li, F.; Tang, B. Z. A Near-Infrared AIEgen for Specific Imaging of Lipid Droplets. *Chem. Commun.* **2016**, *52*, 5957−5960.
(29) Wang, Y. J.; Shi, Y.; Wang, Z.; Zhu, Z.; Zhao, X.; Nie, H.; Qian, J.; Qin, A.; Sun, J. Z.; Tang, B. Z. A Red to Near-IR Fluorogen: Aggregation-Induced Emission, Large Stokes Shift, High Solid Efficiency and Application in Cell-Imaging. *Chem. - Eur. J.* **2016**, *22*, 9784−9791.
(30) Gao, Y.; Feng, G.; Jiang, T.; Goh, C.; Ng, L.; Liu, B.; Li, B.; Yang, L.; Hua, J.; Tian, H. Biocompatible Nanoparticles Based on Diketo-Pyrrolo-Pyrrole (DPP) with Aggregation-Induced Red/NIR Emission for *in Vivo* Two-Photon Fluorescence Imaging. *Adv. Funct. Mater.* **2015**, *25*, 2857−2866.
(31) Lu, H.; Zheng, Y.; Zhao, X.; Wang, L.; Ma, S.; Han, X.; Xu, B.; Tian, W.; Gao, H. Highly Efficient Far Red/Near-Infrared Solid Fluorophores: Aggregation-Induced Emission, Intramolecular Charge Transfer, Twisted Molecular Conformation, and Bioimaging Applications. *Angew. Chem., Int. Ed.* **2016**, *55*, 155−159.
(32) Shao, A.; Xie, Y.; Zhu, S.; Guo, Z.; Zhu, S.; Guo, J.; Shi, P.; James, T. D.; Tian, H.; Zhu, W. H. Far-Red and Near-IR AIE-Active Fluorescent Organic Nanoprobes with Enhanced Tumor-Targeting Efficacy: Shape-Specific Effects. *Angew. Chem., Int. Ed.* **2015**, *54*, 7383−7388.
(33) Yan, L.; Zhang, Y.; Xu, B.; Tian, W. Fluorescent Nanoparticles Based on AIE Fluorogens for Bioimaging. *Nanoscale* **2016**, *8*, 2471−2487.
(34) Yang, J.; Gao, Y.; Jiang, T.; Liu, W.; Liu, C.; Lu, N.; Li, B.; Mei, J.; Peng, Q.; Hua, J. Substituent Effects on the Aggregation-Induced Emission and Two-Photon Absorption Properties of Triphenylamine−dibenzo [a, c] phenazine adducts. *Mater. Chem. Front.* **2017**, *1*, 1396−1405.
(35) Ding, D.; Li, K.; Qin, W.; Zhan, R.; Hu, Y.; Liu, J.; Tang, B. Z.; Liu, B. Conjugated Polymer Amplified Far-Red/Near-Infrared Fluorescence from Nanoparticles with Aggregation-Induced Emission Characteristics for Targeted *in Vivo* Imaging. *Adv. Healthcare Mater.* **2013**, *2*, 500−507.
(36) Yuan, Y.; Feng, G.; Qin, W.; Tang, B. Z.; Liu, B. Targeted and Image-Guided Photodynamic Cancer Therapy Based on Organic Nanoparticles with Aggregation-Induced Emission Characteristics. *Chem. Commun.* **2014**, *50*, 8757−8760.
(37) Wu, W.; Mao, D.; Hu, F.; Xu, S.; Chen, C.; Zhang, C. J.; Cheng, X.; Yuan, Y.; Ding, D.; Kong, D.; et al. A Highly Efficient and Photostable Photosensitizer with Near-Infrared Aggregation-Induced Emission for Image-Guided Photodynamic Anticancer Therapy. *Adv. Mater.* **2017**, *29*, 1700548.
(38) Zipfel, W. R.; Williams, R. M.; Webb, W. W. Nonlinear Magic: Multiphoton Microscopy in the Biosciences. *Nat. Biotechnol.* **2003**, *21*, 1369−1377.
(39) Kim, H. M.; Cho, B. R. Small-Molecule Two-Photon Probes for Bioimaging Applications. *Chem. Rev.* **2015**, *115*, 5014−5055.
(40) Lou, X.; Zhao, Z.; Tang, B. Z. Organic Dots Based on AIEgens for Two-Photon Fluorescence Bioimaging. *Small* **2016**, *12*, 6430−6450.
(41) Zhen, S.; Wang, S.; Li, S.; Luo, W.; Gao, M.; Ng, L. G.; Goh, C. C.; Qin, A.; Zhao, Z.; Liu, B.; et al. Efficient Red/Near-Infrared Fluorophores Based on Benzo [1, 2-b: 4, 5-b′] dithiophene 1, 1, 5, 5−Tetraoxide for Targeted Photodynamic Therapy and *in Vivo* Two-Photon Fluorescence Bioimaging. *Adv. Funct. Mater.* **2018**, *28*, 1706945.
(42) Blom, T.; Somerharju, P.; Ikonen, E. Synthesis and Biosynthetic Trafficking of Membrane Lipids. *Cold Spring Harbor Perspect. Biol.* **2011**, *3*, a004713.
(43) Zehmer, J. K.; Huang, Y.; Peng, G.; Pu, J.; Anderson, R. G.; Liu, P. A Role for Lipid Droplets in Inter-Membrane Lipid Traffic. *Proteomics* **2009**, *9*, 914−921.
(44) Farese, R. V., Jr; Walther, T. C. Lipid Droplets Finally Get a Little RESPECT. *Cell* **2009**, *139*, 855−860.
(45) Martin, S.; Parton, R. G. Opinion: Lipid Droplets: a Unified View of a Dynamic Organelle. *Nat. Rev. Mol. Cell Biol.* **2006**, *7*, 373.
(46) Greenberg, A. S.; Coleman, R. A.; Kraemer, F. B.; McManaman, J. L.; Obin, M. S.; Puri, V.; Yan, Q. W.; Miyoshi, H.; Mashek, D. G. The Role of Lipid Droplets in Metabolic Disease in Rodents and Humans. *J. Clin. Invest.* **2011**, *121*, 2102−2110.
(47) Olzmann, J. A.; Richter, C. M.; Kopito, R. R. Spatial Regulation of UBXD8 and p97/VCP Controls ATGL-Mediated Lipid Droplet Turnover. *Proc. Natl. Acad. Sci. U. S. A.* **2013**, *110*, 1345−1350.
(48) Walther, T. C.; Farese, R. V., Jr Lipid Droplets and Cellular Lipid Metabolism. *Annu. Rev. Biochem.* **2012**, *81*, 687−714.
(49) Thiam, A. R.; Farese, R. V., Jr; Walther, T. C. The Biophysics and Cell Biology of Lipid Droplets. *Nat. Rev. Mol. Cell Biol.* **2013**, *14*, 775−786.
(50) Bozza, P. T.; Viola, J. P. Lipid Droplets in Inflammation and Cancer. *Prostaglandins, Leukotrienes Essent. Fatty Acids* **2010**, *82*, 243−250.
(51) Krahmer, N.; Farese, R. V.; Walther, T. C. Balancing the Fat: Lipid Droplets and Human Disease. *EMBO Mol. Med.* **2013**, *5*, 973−983.
(52) Herker, E.; Harris, C.; Hernandez, C.; Carpentier, A.; Kaehlcke, K.; Rosenberg, A. R.; Farese, R. V., Jr; Ott, M. Efficient Hepatitis C Virus Particle Formation Requires Diacylglycerol Acyltransferase-1. *Nat. Med.* **2010**, *16*, 1295−1298.
(53) Tirinato, L.; Pagliari, F.; Limongi, T.; Marini, M.; Falqui, A.; Seco, J.; Candeloro, P.; Liberale, C.; Di Fabrizio, E. An Overview of Lipid Droplets in Cancer and Cancer Stem Cells. *Stem Cells Int.* **2017**, *2017*, 1.
(54) Liu, Q.; Luo, Q.; Halim, A.; Song, G. Targeting Lipid Metabolism of Cancer Cells: A Promising Therapeutic Strategy for Cancer. *Cancer Lett.* **2017**, *401*, 39−45.
(55) Abramczyk, H.; Surmacki, J.; Kopeć, M.; Olejnik, A. K.; Lubecka-Pietruszewska, K.; Fabianowska-Majewska, K. The Role of Lipid Droplets and Adipocytes in Cancer. Raman Imaging of Cell Cultures: MCF10A, MCF7, and MDA-MB-231 Compared to Adipocytes in Cancerous Human Breast Tissue. *Analyst* **2015**, *140*, 2224−2235.
(56) Duchen, M. R. Mitochondria in Health and Disease: Perspectives on a New Mitochondrial Biology. *Mol. Aspects Med.* **2004**, *25*, 365−451.

DOI: 10.1021/acsnano.8b03138
ACS Nano 2018, 12, 8145−8159

(57) Lin, M. T.; Beal, M. F. Mitochondrial Dysfunction and Oxidative Stress in Neurodegenerative Diseases. *Nature* **2006**, *443*, 787−795.
(58) Hayashi, J. I.; Ohta, S.; Kikuchi, A.; Takemitsu, M.; Goto, Y. I.; Nonaka, I. Introduction of Disease-Related Mitochondrial DNA Deletions into HeLa Cells Lacking Mitochondrial DNA Results in Mitochondrial Dysfunction. *Proc. Natl. Acad. Sci. U. S. A.* **1991**, *88*, 10614−10618.
(59) Abou-Sleiman, P. M.; Muqit, M. M.; Wood, N. W. Expanding Insights of Mitochondrial Dysfunction in Parkinson's Disease. *Nat. Rev. Neurosci.* **2006**, *7*, 207−219.
(60) Wongrakpanich, A.; Geary, S. M.; Joiner, M.-l. A.; Anderson, M. E.; Salem, A. K. Mitochondria-Targeting Particles. *Nanomedicine* **2014**, *9*, 2531−2543.
(61) Decaudin, D.; Marzo, I.; Brenner, C.; Kroemer, G. Mitochondria in Chemotherapy-Induced Apoptosis: a Prospective Novel Target of Cancer Therapy. *Int. J. Oncol.* **1998**, *12*, 141−193.
(62) Zhang, D.; Wen, L.; Huang, R.; Wang, H.; Hu, X.; Xing, D. Mitochondrial Specific Photodynamic Therapy by Rare-Earth Nanoparticles Mediated Near-Infrared Graphene Quantum Dots. *Biomaterials* **2018**, *153*, 14−26.
(63) Chakrabortty, S.; Agrawalla, B. K.; Stumper, A.; Vegi, N. M.; Fischer, S.; Reichardt, C.; Kögler, M.; Dietzek, B.; Feuring-Buske, M.; Buske, C.; et al. Mitochondria Targeted Protein-Ruthenium Photosensitizer for Efficient Photodynamic Applications. *J. Am. Chem. Soc.* **2017**, *139*, 2512−2519.
(64) Ryan, T.; Chris, W.; Jacky, W.; ZhongáTang, B. A Near-Infrared AIEgen for Specific Imaging of Lipid Droplets. *Chem. Commun.* **2016**, *52*, 5957−5960.
(65) Gao, M.; Su, H.; Lin, Y.; Ling, X.; Li, S.; Qin, A.; Tang, B. Z. Photoactivatable Aggregation-Induced Emission Probes for Lipid Droplets-Specific Live Cell Imaging. *Chem. Sci.* **2017**, *8*, 1763−1768.
(66) Jiang, M.; Gu, X.; Lam, J. W.; Zhang, Y.; Kwok, R. T.; Wong, K. S.; Tang, B. Z. Two-Photon AIE Bio-Probe with Large Stokes Shift for Specific Imaging of Lipid Droplets. *Chem. Sci.* **2017**, *8*, 5440−5446.
(67) Wang, D.; Su, H.; Kwok, R. T.; Shan, G.; Leung, A.; Lee, M.; Sung, H. H.; Williams, I. D.; Lam, J. W.; Tang, B. Z. Facile Synthesis of Red/NIR AIE Luminogens with Simple Structures, Bright Emissions, and High Photostabilities, and Their Applications for Specific Imaging of Lipid Droplets and Image-Guided Photodynamic Therapy. *Adv. Funct. Mater.* **2017**, *27*, 1704039.
(68) Collot, M.; Fam, T. K.; Ashokkumar, P.; Faklaris, O.; Galli, T.; Danglot, L.; Klymchenko, A. S. Ultrabright and Fluorogenic Probes for Multicolor Imaging and Tracking of Lipid Droplets in Cells and Tissues. *J. Am. Chem. Soc.* **2018**, *140*, 5401−5411.
(69) He, G. S.; Tan, L. S.; Zheng, Q.; Prasad, P. N. Multiphoton Absorbing Materials: Molecular Designs, Characterizations, and Applications. *Chem. Rev.* **2008**, *108*, 1245−1330.
(70) Pawlicki, M.; Collins, H. A.; Denning, R. G.; Anderson, H. L. Two-Photon Absorption and the Design of Two-Photon Dyes. *Angew. Chem., Int. Ed.* **2009**, *48*, 3244−3266.
(71) Zheng, Z.; Yu, Z.; Yang, M.; Jin, F.; Zhang, Q.; Zhou, H.; Wu, J.; Tian, Y. Substituent Group Variations Directing the Molecular Packing, Electronic Structure, and Aggregation-Induced Emission Property of Isophorone Derivatives. *J. Org. Chem.* **2013**, *78*, 3222−3234.
(72) Gao, M.; Su, H.; Li, S.; Lin, Y.; Ling, X.; Qin, A.; Tang, B. Z. An Easily Accessible Aggregation-Induced Emission Probe for Lipid Droplet-Specific Imaging and Movement Tracking. *Chem. Commun.* **2017**, *53*, 921−924.
(73) Xu, S.; Yuan, Y.; Cai, X.; Zhang, C.-J.; Hu, F.; Liang, J.; Zhang, G.; Zhang, D.; Liu, B. Tuning the Singlet-Triplet Energy Gap: a Unique Approach to Efficient Photosensitizers with Aggregation-Induced Emission (AIE) Characteristics. *Chem. Sci.* **2015**, *6*, 5824−5830.
(74) Massin, J.; Charaf-Eddin, A.; Appaix, F.; Bretonnière, Y.; Jacquemin, D.; van der Sanden, B.; Monnereau, C.; Andraud, C. A Water Soluble Probe with Near Infrared Two-Photon Absorption and Polarity-Induced Fluorescence for Cerebral Vascular Imaging. *Chem. Sci.* **2013**, *4*, 2833−2843.
(75) Sumalekshmy, S.; Fahrni, C. J. Metal-Ion-Responsive Fluorescent Probes for Two-Photon Excitation Microscopy. *Chem. Mater.* **2011**, *23*, 483−500.
(76) Zhang, R.; Sun, Y.; Tian, M.; Zhang, G.; Feng, R.; Li, X.; Guo, L.; Yu, X.; Sun, J. Z.; He, X. Phospholipid-Biomimetic Fluorescent Mitochondrial Probe with Ultrahigh Selectivity Enables *in Situ* and High-Fidelity Tissue Imaging. *Anal. Chem.* **2017**, *89*, 6575−6582.
(77) Singh, A.; Kim, W.; Kim, Y.; Jeong, K.; Kang, C. S.; Kim, Y.; Koh, J.; Mahajan, S. D.; Prasad, P. N.; Kim, S. Multifunctional Photonics Nanoparticles for Crossing the Blood−Brain Barrier and Effecting Optically Trackable Brain Theranostics. *Adv. Funct. Mater.* **2016**, *26*, 7057−7066.
(78) Apel, K.; Hirt, H. Reactive Oxygen Species: Metabolism, Oxidative Stress, and Signal Transduction. *Annu. Rev. Plant Biol.* **2004**, *55*, 373−399.
(79) DeRosa, M. C.; Crutchley, R. J. Photosensitized Singlet Oxygen and Its Applications. *Coord. Chem. Rev.* **2002**, *233*, 351−371.
(80) Kearns, D. R. Physical and Chemical Properties of Singlet Molecular Oxygen. *Chem. Rev.* **1971**, *71*, 395−427.
(81) Xu, Y.; He, R.; Lin, D.; Ji, M.; Chen, J. Laser Beam Controlled Drug Release from Ce6−Gold Nanorod Composites in Living Cells: a FLIM Study. *Nanoscale* **2015**, *7*, 2433−2441.
(82) Meng, Z.; Yu, B.; Han, G.; Liu, M.; Shan, B.; Dong, G.; Miao, Z.; Jia, N.; Tan, Z.; Li, B.; et al. Chlorin p6-Based Water-Soluble Amino Acid Derivatives as Potent Photosensitizers for Photodynamic Therapy. *J. Med. Chem.* **2016**, *59*, 4999−5010.
(83) Inukai, N.; Kawai, T.; Yuasa, J. One-Step *Versus* Multistep Equilibrium of Carbazole-Bridged Dinuclear Zinc (II) Complex Formation: Metal-Assisted π-Association and-Dissociation Processes. *Chem. - Eur. J.* **2014**, *20*, 15159−15168.
(84) Zhao, N.; Li, M.; Yan, Y.; Lam, J. W.; Zhang, Y. L.; Zhao, Y. S.; Wong, K. S.; Tang, B. Z. A Tetraphenylethene-Substituted Pyridinium Salt with Multiple Functionalities: Synthesis, Stimuli-Responsive Emission, Optical Waveguide and Specific Mitochondrion Imaging. *J. Mater. Chem. C* **2013**, *1*, 4640−4646.
(85) Ford, J. A., Jr; Wilson, C. V.; Young, W. R. The Preparation of 2 (5H)-Furanones and Dyes Derived from Them. *J. Org. Chem.* **1967**, *32*, 173−177.

DOI: 10.1021/acsnano.8b03138
ACS Nano 2018, 12, 8145−8159